ADVANCING EARTH AND SPACE SCIENCE

JGR Solid Earth

RESEARCH ARTICLE
10.1029/2021JB022983

Key Points:

- We present the line-of-sight gravity difference (LGD) gravimetric data product from GRACE Follow-On (GRACE-FO) inter-satellite laser ranging measurements
- LGD observations from laser ranging measurements clearly detect rapid (sub-monthly) mass change signals in the Earth system
- Along-orbit analysis of inter-satellite ranging data can broaden the scope of geophysical applications from GRACE-FO

Supporting Information:

Supporting Information may be found in the online version of this article.

Correspondence to:

K. Ghobadi-Far,
khosro@vt.edu

Citation:

Ghobadi-Far, K., Han, S.-C., McCullough, C. M., Wiese, D. N., Ray, R. D., Sauber, J., et al. (2022). Along-orbit analysis of GRACE Follow-On inter-satellite laser ranging measurements for sub-monthly surface mass variations. *Journal of Geophysical Research: Solid Earth*, *127*, e2021JB022983. https://doi.org/10.1029/2021JB022983

Received 11 AUG 2021
Accepted 21 JAN 2022

Along-Orbit Analysis of GRACE Follow-On Inter-Satellite Laser Ranging Measurements for Sub-Monthly Surface Mass Variations

Khosro Ghobadi-Far[1,2], Shin-Chan Han[1], Christopher M. McCullough[3], David N. Wiese[3], Richard D. Ray[4], Jeanne Sauber[4], Linus Shihora[5], and Henryk Dobslaw[5]

[1]School of Engineering, University of Newcastle, Newcastle, NSW, Australia, [2]Now at Department of Geosciences, Virginia Tech, Blacksburg, VA, USA, [3]Jet Propulsion Laboratory, California Institute of Technology, Pasadena, CA, USA, [4]NASA Goddard Space Flight Center, Geodesy and Geophysics Laboratory, Greenbelt, MD, USA, [5]GFZ German Research Centre for Geosciences, Department 1: Geodesy and Remote Sensing, Potsdam, Germany

Abstract We examined the sensitivity of GRACE Follow-On (GRACE-FO) laser ranging interferometer (LRI) measurements to sub-monthly time-variable gravity (TVG) signals caused by transient, high-frequency mass changes in the Earth system. GRACE-FO LRI provides complementary inter-satellite ranging measurements with higher precision over a wider range of frequencies than the baseline K-band microwave ranging system. The common approach for studying mass variation relies on the inverted TVG or mascon solutions over a period of, for example, one month or 10 days which are adversely affected by temporal aliasing and/or smoothing. In this article, we present the alternative along-orbit analysis methodology in terms of line-of-sight gravity difference (LGD) to fully exploit the higher precision LRI measurements for examination of sub-monthly mass changes. The discrepancy between "instantaneous" LGD LRI observations and monthly-mean LGD (from Level-2 data) at satellite altitude indicates the sub-monthly gravitational variability not captured by monthly-mean solutions. In conjunction with the satellite ocean altimetry observations, high-frequency non-tidal atmosphere and ocean models, and hydrology models, we show that the LGD LRI observations detect the high-frequency oceanic mass variability in the Argentine Basin and the Gulf of Carpentaria, and sub-monthly variations in surface (river) water in the Amazon Basin. We demonstrate the benefits gained from repeat ground track analysis of GRACE-FO LRI data in the case of the Amazon surface water flow. The along-orbit analysis methodology based on LGD LRI time series presented here is especially suitable for quantifying temporal and spatial evolution of extreme, rapidly changing mass variations.

Plain Language Summary The GRACE Follow-On (GRACE-FO) mission, launched on 22 May 2018, is extending the legacy of GRACE by measuring time-variable gravity field of the Earth. Temporal variation in Earth gravity field is caused by mass change on and near the Earth surface due to various processes in hydrosphere, cryosphere, solid Earth, and ocean. In addition to the Ka-band ranging system, the GRACE-FO satellites are also equipped with a laser ranging interferometer (LRI) which measures the inter-satellite distance change with higher precision. When GRACE-FO satellites fly over a mass change anomaly, the LRI measurements capture the corresponding gravitational changes at ~500 km altitude. We directly examine the LRI gravitational measurements and show that they clearly detect the rapid mass variability associated with the high-frequency (a) oceanic gyre in the Argentine Basin, (b) oceanic mass changes in the Gulf of Carpentaria, and (c) river water variation in the Amazon Basin. Such processes show large mass variability within a month and, thus, they cannot be adequately studied using the standard monthly-mean data products from GRACE-FO mission. Therefore, the presented along-orbit analysis approach broadens the scope of geophysical applications that can be addressed by GRACE-FO satellites data.

1. Introduction

The Gravity Recovery and Climate Experiment Follow-On (GRACE-FO) mission (Landerer et al., 2020), launched on 22 May 2018, is extending the GRACE data record (2002–2017; Tapley et al., 2004) of global mass transport and provides a unique perspective into Earth's evolving climate and water cycle. The monthly-mean time-variable gravity (TVG) fields from GRACE and GRACE-FO with a spatial resolution of 300–500 km are routinely used to monitor and study mass changes caused by solid Earth, oceanic, atmospheric, hydrologic, and

cryospheric processes (Tapley et al., 2019). The microwave-based K-band ranging (KBR) measurements with μm precision are used to compute the standard GRACE and GRACE-FO monthly-mean TVG data along with orbit, orientation, and non-gravitational accelerometer data.

As a technology demonstration of inter-satellite ranging by optical lasers aimed for future GRACE-like missions, GRACE-FO is also equipped with a laser ranging interferometer (LRI) which measures the inter-satellite distance with nm precision (Sheard et al., 2012). The GRACE-FO LRI has been providing the first laser interferometric range measurements between remote spacecraft since June 2018 with a noise level of 1 nm/$\sqrt{\text{Hz}}$ at frequencies above 100 mHz (Abich et al., 2019). The LRI measurements have the potential to improve the sensitivity to near-surface mass variations, especially if coupled with next-generation accelerometers with higher precision for measurement of non-gravitational forces acting on the satellites (Kang & Bender, 2021; Spero, 2021).

The monthly-mean TVG (Level-2; L2) and mascon (Level-3; L3) solutions are estimated by inversion of inter-satellite range-rate residuals. The residuals are obtained by subtracting the static gravity as well as high-frequency (sub-monthly) geophysical signals like ocean tides and non-tidal atmosphere and ocean mass variability (given by the so-called AOD1B models [e.g., Dobslaw et al., 2017]) from measured KBR and LRI measurements (Yuan, 2019). As such, the errors in KBR and LRI residuals originate from sensor (KBR, LRI, and accelerometer) noise as well as errors in high-frequency background models like AOD1B. Since the early years of GRACE, it was well established that mis-/un-modeled errors in high-frequency background models exceed the sensor noise and, therefore, dominate the monthly-mean solutions (e.g., Han et al., 2004). That is why despite the much lower noise level of LRI, especially at higher frequencies, the L2 solutions obtained from GRACE-FO KBR and LRI are of comparable quality (e.g., Fahnestock et al., 2019; Flechtner et al., 2016). Thus, analysis of laser tracking data in terms of standard monthly-mean L2/L3 solutions does not allow for fully exploiting the higher precision LRI measurements.

To fully demonstrate the advantage gained from LRI, Ghobadi-Far, Han, McCullough, et al. (2020) employed a novel method of directly analyzing inter-satellite ranging residuals along the satellite orbit and showed that, relative to KBR, LRI improves the accuracy of gravitational measurements by as much as one order of magnitude at frequencies above 10 mHz. The spectrum of LRI residuals at higher frequencies is dominated by mis-/un-modeled static gravity signals. In this article, we present the along-orbit analysis methodology for the examination of TVG and surface mass change (SMC) signals. The along-orbit analysis is particularly suitable for examining high-frequency (sub-monthly) mass variations because inter-satellite ranging residuals represent *instantaneous* gravitational changes caused by mass change happening at or beneath the Earth surface. In contrast to the monthly-mean TVG or mascon solutions, which are most appropriate for monitoring seasonal to interannual changes, our approach in this study could be used to examine geophysical processes associated with significantly shorter time-scales, such as tsunamis (Ghobadi-Far, Han, Allgeyer, et al., 2020) and Earth free oscillations (Ghobadi-Far et al., 2019).

Our methodology is based on along-orbit analysis of observations and models in terms of line-of-sight gravity difference (LGD). We first describe the formula for computation of synthetic LGD from TVG fields and SMC grids (available from gravity and geophysical models), and discuss the effect of elastic loading (Section 2). The LGD observations are computed from inter-satellite ranging residuals. We review and further validate the LGD approach, originally developed by Ghobadi-Far et al. (2018) for GRACE KBR analysis, for representation of instantaneous TVG signals at satellite altitude from LRI measurements (Section 3). The discrepancy between synthetic LGD obtained from monthly-mean L2 solutions and LGD observations from LRI measurements indicates sub-monthly mass variability. We present three examples of such high-frequency (sub-monthly) oceanic and hydrologic mass changes detected by precise LRI measurements (Section 4): oceanic mass variability in (a) the Argentine Basin and (b) Gulf of Carpentaria (GoC), and (c) surface water transport in the Amazon River Basin. We verify the above rapid mass changes using ocean altimetry data, a test release for the next AOD1B model and the GLDAS/NOAH hydrology model. We conclude by presenting our perspective on the use of LRI data for various sub-monthly applications (Section 5).

The aim of this article is to demonstrate the sensitivity of LRI to high-frequency mass variations with different kinds of examples and develop a new methodology of exploiting such LRI measurements for studying high-frequency geophysical processes that are not captured by the standard L2 and L3 data products from the GRACE-FO project.

2. Synthetic LGD Computation From Time-Variable Gravity and Surface Mass Change Models

LGD is defined as the difference of two gravity vectors exerted on the twin GRACE-FO satellites projected in the line-of-sight (LOS) direction. We provide the equations to compute LGD from TVG fields and SMC grids in this section. The two methods of computing LGD from TVG and SMC data are essentially equivalent. Nonetheless, we still find it useful to provide the equations for both approaches so that one can directly compute LGD from either data types without the need to convert one to the other.

2.1. LGD From TVG Fields

Geopotential fields representing TVG are conventionally given in terms of anomalous spherical harmonic coefficients $\delta\bar{C}_{lm}$ and $\delta\bar{S}_{lm}$ to the maximum degree L. Geopotential change δV along the satellite orbit at position (r, φ, λ) as a series in spherical harmonics reads (Heiskanen & Moritz, 1967):

$$\delta V(r,\varphi,\lambda) = \frac{GM}{R}\sum_{l=0}^{L}\left(\frac{R}{r}\right)^{l+1}\sum_{m=0}^{l}\left[\delta\bar{C}_{lm}\ \cos(m\lambda) + \delta\bar{S}_{lm}\ \sin(m\lambda)\right]\bar{P}_{lm}(\sin\varphi), \tag{1}$$

where GM is the gravitational constant times the Earth's mass, R is the Earth equatorial radius, and $\bar{P}_{lm}$ is the normalized associated Legendre function of degree l and order m. The gravity vector in the local North-East-Up (NEU) frame is given by (e.g., Koop, 1993):

$$\begin{bmatrix}\delta V_N(r,\varphi,\lambda)\\ \delta V_E(r,\varphi,\lambda)\\ \delta V_U(r,\varphi,\lambda)\end{bmatrix} = \frac{GM}{R^2}\begin{bmatrix}\sum_{l=0}^{L}\left(\frac{R}{r}\right)^{l+2}\sum_{m=0}^{l}\left[\delta\bar{C}_{lm}\cos(m\lambda)+\delta\bar{S}_{lm}\sin(m\lambda)\right]\bar{P}'_{lm}(\sin\varphi)\\ \frac{1}{\cos\varphi}\sum_{l=0}^{L}\left(\frac{R}{r}\right)^{l+2}\sum_{m=0}^{l}\left[-\delta\bar{C}_{lm}\sin(m\lambda)+\delta\bar{S}_{lm}\cos(m\lambda)\right]\bar{P}_{lm}(\sin\varphi)\\ \sum_{l=0}^{L}\left(\frac{R}{r}\right)^{l+2}\{-(l+1)\}\sum_{m=0}^{l}\left[\delta\bar{C}_{lm}\cos(m\lambda)+\delta\bar{S}_{lm}\sin(m\lambda)\right]\bar{P}_{lm}(\sin\varphi)\end{bmatrix}, \tag{2}$$

With $\bar{P}'_{lm}$ being the derivative of $\bar{P}_{lm}$. The LGD computation requires the gravity and LOS unit vector to be expressed in the same coordinate frame. The LOS unit vector is simply given in the Earth-Centered Earth-Fixed (ECEF) frame by $\boldsymbol{e}_{12}^{\mathrm{LOS}} = \frac{\boldsymbol{r}_2-\boldsymbol{r}_1}{|\boldsymbol{r}_2-\boldsymbol{r}_1|}$, with $\boldsymbol{r}_1$ and $\boldsymbol{r}_2$ denoting the ECEF position vectors of GRACE-FO satellites. The rotation matrix from NEU to ECEF is given by:

$$\mathbb{R} = \begin{bmatrix}-\sin\varphi\cos\lambda & -\sin\lambda & \cos\varphi\cos\lambda\\ -\sin\varphi\sin\lambda & \cos\lambda & \cos\varphi\sin\lambda\\ \cos\varphi & 0 & \sin\varphi\end{bmatrix}. \tag{3}$$

The gravity vector in ECEF is obtained by $\delta\boldsymbol{g}^{\mathrm{ECEF}} = \mathbb{R}\delta\boldsymbol{g}^{\mathrm{NEU}}$, where $\delta\boldsymbol{g}^{\mathrm{NEU}} = [\delta V_N\ \delta V_E\ \delta V_U]^T$ and $\delta\boldsymbol{g}^{\mathrm{ECEF}} = [\delta V_X\ \delta V_Y\ \delta V_Z]^T$. The synthetic LGD from the TVG models is then computed as:

$$\delta g_{12}^{\mathrm{LOS}} = \left(\delta\boldsymbol{g}_2^{\mathrm{ECEF}} - \delta\boldsymbol{g}_1^{\mathrm{ECEF}}\right)\cdot\boldsymbol{e}_{12}^{\mathrm{LOS}}, \tag{4}$$

where "." denotes the inner product.

2.2. LGD From SMC Grids

SMC data are given in the form of a grid on the surface of the Earth in terms of equivalent water height in for example, meter. The GRACE-FO satellites sense the direct gravitational attraction by the surface mass as well

as solid Earth deformation caused by the mass loading. In the following, by approximating each cell of the SMC grid by a point-mass, we present the LGD computation method using numerical integration, first without and then with inclusion of the elastic loading effect.

2.2.1. LGD From SMC Grids Without the Loading Effect

Geopotential change δV_i at the altitude of GRACE-FO satellite i ($i = 1$ or 2) caused by the SMC grid including a total of J point-masses is given by (Heiskanen & Moritz, 1967):

$$\delta V_i = G \sum_{j=1}^{J} \frac{\delta m_j}{d_{ij}}, \tag{5}$$

where d_{ij} is the distance between the point-mass j and satellite i. δm in terms of equivalent water height h is written as $\delta m_j = h_j \rho_w R^2 \Delta\varphi \Delta\lambda \cos\varphi_j$, with ρ_w being the volumetric density of water in kg/m^3, and $\Delta\varphi$ and $\Delta\lambda$ being the grid interval (spatial resolution) of the SMC grid in the latitude and longitude directions, respectively. Defining the ECEF coordinates of point-mass j and satellite i as $\left[X_j\, Y_j\, Z_j\right]^{\mathrm{T}}$ and $[X_i\, Y_i\, Z_i]^{\mathrm{T}}$, respectively, the gravity difference vector between two GRACE-FO satellites in the ECEF frame is formulated as (Heiskanen & Moritz, 1967):

$$\delta \boldsymbol{g}_2^{\mathrm{ECEF}} - \delta \boldsymbol{g}_1^{\mathrm{ECEF}} = G \sum_{j=1}^{J} \delta m_j \begin{bmatrix} \dfrac{X_2 - X_j}{d_{2j}^3} - \dfrac{X_1 - X_j}{d_{1j}^3} \\ \dfrac{Y_2 - Y_j}{d_{2j}^3} - \dfrac{Y_1 - Y_j}{d_{1j}^3} \\ \dfrac{Z_2 - Z_j}{d_{2j}^3} - \dfrac{Z_1 - Z_j}{d_{1j}^3} \end{bmatrix}. \tag{6}$$

LGD caused by SMC grid is obtained by substituting Equation 6 in Equation 4.

2.2.2. LGD From SMC Grids Considering the Loading Effect

To include the loading effect in the LGD computation from SMC grids, we reformulate the geopotential δV in Equation 5 into a spectral form to incorporate the potential load Love numbers k_l (Farrell, 1972). Such spectral form can be obtained by expressing the inverse distance $1/d$ in terms of the Legendre polynomials P_n (Heiskanen & Moritz, 1967):

$$\delta V_i = G \sum_{j=1}^{J} \frac{\delta m_j}{R} \sum_{l=0}^{\infty} \left(1 + k_l\right) \left(\frac{R}{r}\right)^{l+1} P_l\left(\cos\psi_{ij}\right), \tag{7}$$

where ψ_{ij} is the spherical (angular) distance between the point-mass j and satellite i, given by:

$$\cos\psi_{ij} = \sin\varphi_i \sin\varphi_j + \cos\varphi_i \cos\varphi_j \cos\left(\lambda_i - \lambda_j\right). \tag{8}$$

The gravity vector in the NEU frame is given by:

$$\begin{bmatrix} \delta V_{iN}(r, \varphi, \lambda) \\ \delta V_{iE}(r, \varphi, \lambda) \\ \delta V_{iU}(r, \varphi, \lambda) \end{bmatrix} = \frac{G}{R^2} \begin{bmatrix} \sum_{j=1}^{J} \delta m_j \sum_{l=0}^{\infty} (1 + k_l) \left(\frac{R}{r_i}\right)^{l+2} \frac{d\cos\psi_{ij}}{d\varphi_i} P_n'(\cos\psi_{ij}) \\ \sum_{j=1}^{J} \frac{\delta m_j}{\cos\varphi_i} \sum_{l=0}^{\infty} (1 + k_l) \left(\frac{R}{r_i}\right)^{l+2} \frac{d\cos\psi_{ij}}{d\lambda_i} P_n'(\cos\psi_{ij}) \\ \sum_{j=1}^{J} -\delta m_j \sum_{l=0}^{\infty} (1 + k_l)(l+1) \left(\frac{R}{r_i}\right)^{l+2} P_n(\cos\psi_{ij}) \end{bmatrix}, \tag{9}$$

where P_n' is the derivative of the Legendre polynomial. LGD is obtained by transformation of the NEU gravity vectors to ECEF and then projection of the gravity difference vector in the LOS direction, using Equations 3 and 4.

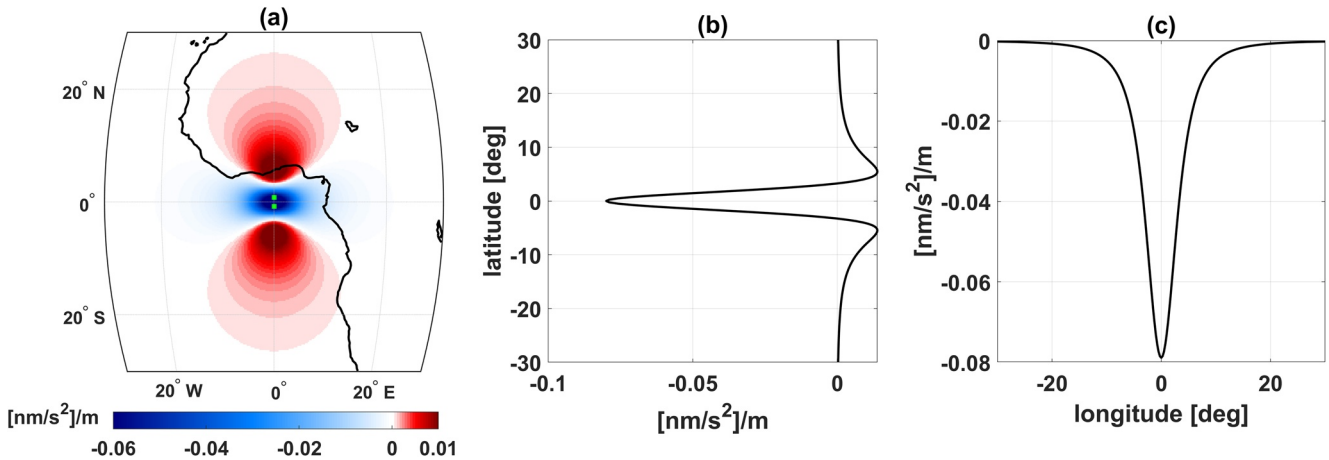

Figure 1. Sensitivity analysis of the LGD kernel evaluated at 490 km altitude for a case where the barycenter of GRACE(-FO) satellites is located at latitude 0° and longitude 0°. (a) Kernel values in [nm/s^2]/m along with the positions of the GRACE(-FO) satellites denoted by green squares. (b) Cross-sectional view of the kernel along the meridian. (c) Cross-sectional view of the kernel along the equator. The larger the kernel value at a certain position, the larger the contribution of mass anomaly at that position to LGD signal at satellite altitude. LGD, line-of-sight gravity difference.

2.3. Numerical Experiments

We first examined the spatial behavior of the integral kernel to understand the sensitivity of LGD observations to mass anomalies at the Earth's surface. We computed the kernel values for GRACE-FO satellites (i.e., observation points) at the altitude of 490 km with the barycenter of twin satellites located at the latitude and longitude zero, with an inter-satellite distance of 200 km, and for an equiangular grid with 0.25° resolution at the Earth surface. Figure 1a shows the kernel values in terms of nm/s^2/m, and Figures 1b and 1c show its cross-sectional views along the meridional and equatorial planes passing through the barycenter. The kernel values are defined in such a way that, when multiplied by SMC given in terms of equivalent water height in meter, they provide us with LGD in nm/s^2 at satellite altitude. Thus, a positive mass anomaly beneath the satellites is reflected as a negative LGD anomaly and vice-versa. The LGD kernel has its maxima at the barycenter of GRACE-FO satellites. Expectedly, it decays with increasing distance, approaching zero for spherical distances beyond ~20°. In addition, the kernel is clearly non-isotropic, but it possesses symmetric features with respect to the meridional and equatorial planes.

We used satellite altimetry sea level anomalies from longitude of 65°W to 20°W and latitude of 60°S to 25°S with 0.25° × 0.25° spatial resolution on an arbitrary date (1 April 2001) to carry out some numerical experiments on LGD model computation from SMC grids. To that end, we simulated four GRACE-FO tracks at 490 km altitude over the region (see Figure 2a). We first computed LGD using the spectral form (Equation 9) with various maximum degrees of expansion from 100 to 500 and by setting $k_l = 0$. Comparison with the closed form solution (Equation 6) showed that error of the spectral method for the maximum degrees 100, 200, and 500 is on the order of 10^{-2}, 10^{-6}, and 10^{-13} nm/s^2, respectively. Thus, we recommend the use of maximum degree 200 or larger for LGD computation from SMC grids at the GRACE-FO altitude of 490 km.

Furthermore, to examine the magnitude and behavior of the loading effect in LGD computation, we computed LGD along the four GRACE-FO arcs in Figure 2a using Equation 9, once including the loading effect and once by *turning off* the loading effect (i.e., setting $k_l = 0$). Figure 2b shows the LGD signal caused by mass in solid curves, and the mass plus elastic loading effect in dashed curves. Different colors indicate different ground tracks as shown in Figure 2a. Root-mean-square (RMS) of the elastic loading effect in LGD computation is about 10% of that of total LGD.

We also computed LGD along the arc with longitude 40°W using the original ocean altimetry grid with 0.25° spatial resolution, and after resampling the grid at 0.5°, 1°, and 2° resolutions to determine the suitable grid resolution for LGD computation using numerical integration at GRACE-FO altitude. The LGD signals in Figure 2c and the differences in Figure 2d show that using SMC grids with spatial resolution of 0.5° seems to be a suitable trade-off value between accuracy and computational efficiency, leading to errors less than 0.01 nm/s^2 when compared to the case of grid with 0.25° resolution (except near the edges).

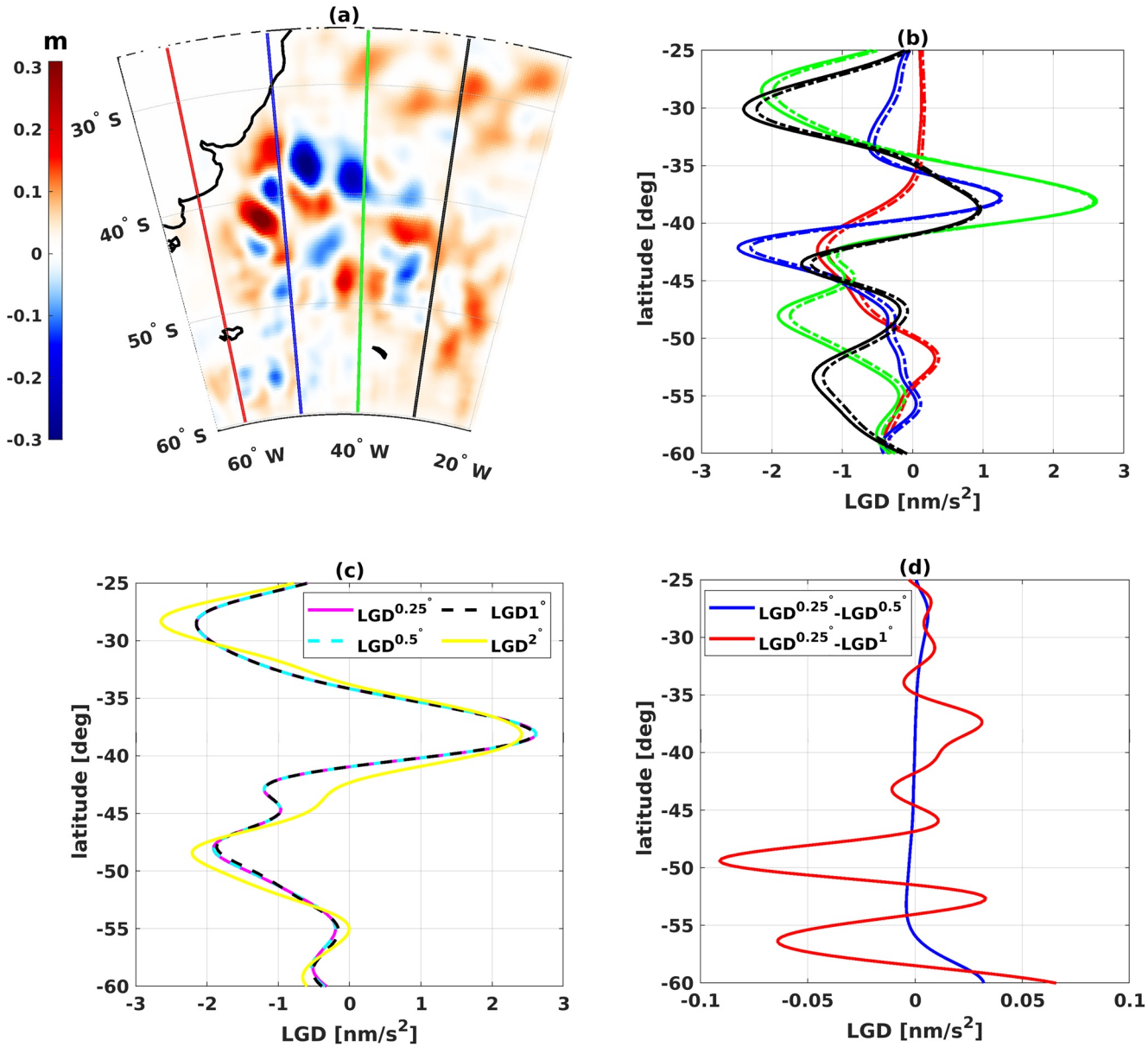

Figure 2. (a) Satellite altimetry measurements of sea surface height (smoothed with a 3° × 3° window) along with four GRACE Follow-On (GRACE-FO) tracks simulated at the altitude of 490 km. (b) Synthetic line-of-sight gravity difference (LGD) time series computed from mass anomalies in (a), considering only the direct mass effect (solid curves) as well as mass plus elastic loading effect (dashed curves). (c) Synthetic LGD along the GRACE-FO track in green in (a) computed from satellite altimetry grid resampled at 0.25° × 0.25°, 0.5° × 0.5°, 1° × 1° and 2° × 2°. (d) Difference between synthetic LGD from 0.25° × 0.25° and 0.5° × 0.5° grids, as well as from 0.25° × 0.25° and 1° × 1° grids. Elastic loading accounts for ∼10% of the total effect. The grid resolution of 0.5° × 0.5° is sufficient to accurately compute LGD from the surface mass grid data at the GRACE-FO altitude of 490 km.

3. LGD Observations From Inter-Satellite Laser Ranging Data

The inter-satellite distance between the two GRACE-FO satellites is measured by the on-board KBR and LRI systems. The measured biased ranges are numerically differentiated and corrected for various effects like light time and ionospheric delay (for KBR only) to obtain instantaneous range-rate measurements. We reduced the inter-satellite range-rate data to residual quantities by removing the calculated range-rate based on the reference orbital state vectors. We used the dynamic reference orbits of the GRACE-FO satellites computed by JPL used for production of the JPL L2 RL06 solutions (Yuan, 2019). Such dynamic orbits were computed by numerically integrating the gravitational potential models including the GGM05C mean gravity field model (Ries et al., 2016),

the high-frequency AOD1B RL06 model (Dobslaw et al., 2017), other well-known geophysical models like ocean tides described in the standard L2 document (Yuan, 2019), as well as non-gravitational forces measured by the on-board accelerometers. As such, our range-rate residuals are the same as the so-called pre-fit range-rate residuals employed for computing the JPL L2 solutions. As the next step, we computed the range-acceleration residuals by numerically differentiating the range-rate residuals using the simple central difference method. The range-acceleration residuals from LRI with a 2 s sampling rate are the key data set used in this study. For a recent GRACE mascon solution based on range-acceleration residuals, see Allgeyer et al. (2022).

Residual range-acceleration $\delta\ddot{\rho}$ and LGD (denoted by $\delta g_{12}^{\mathrm{LOS}}$) are related to each other by the following equation (e.g., Rummel, 1979):

$$\delta\ddot{\rho} = \delta g_{12}^{\mathrm{LOS}} + \delta\left(\dot{\boldsymbol{r}}_{12}\cdot\dot{\boldsymbol{e}}_{12}^{\mathrm{LOS}}\right), \tag{10}$$

where $\dot{\boldsymbol{r}}_{12}$ is the inter-satellite velocity vector. The term $\delta\left(\dot{\boldsymbol{r}}_{12}\cdot\dot{\boldsymbol{e}}_{12}^{\mathrm{LOS}}\right)$ represents the residual centrifugal acceleration difference acting on the satellites. Equation 10 does not include the non-gravitational forces because they were included in the dynamic reference orbits and, thus, were already removed from the observations. The residual non-gravitational forces caused by errors in accelerometer data will be present in the LGD observations, though. Since the residual centrifugal acceleration term is relatively smaller than $\delta\ddot{\rho}$ and mainly contributes to the low frequencies (Ghobadi-Far et al., 2018), LGD was often approximated by range-acceleration residuals (e.g., Spero, 2021; Weigelt, 2017).

Ghobadi-Far et al. (2018) found a spectral relationship between range-acceleration residuals $\delta\ddot{\rho}$ and LGD $\delta g_{12}^{\mathrm{LOS}}$ and developed a transfer function to directly compute $\delta g_{12}^{\mathrm{LOS}}$ from $\delta\ddot{\rho}$ with improved accuracy. Using various cases of synthetic orbit and gravity computation, it was found that $\delta\ddot{\rho}$ and $\delta g_{12}^{\mathrm{LOS}}$ are near-perfectly correlated over frequencies above 1 mHz (or 5 cycles-per-revolution, CPR), and the admittance or transfer function $Z(f)$ between these two quantities is stationary regardless of time, orbital altitude, and the gravitational signal strength and, thus, can be pre-determined from synthetic data. Application of the transfer function $Z(f)$ to $\delta\ddot{\rho}$ is carried out in the frequency domain as follows:

$$\delta g_{12}^{\mathrm{LOS}}(t) = \mathcal{F}^{-1}\left\{Z(f)\cdot\mathcal{F}\left\{\delta\ddot{\rho}(t)\right\}\right\}, \tag{11}$$

where t refers to time of observation, and $\mathcal{F}\{\ldots\}$ and $\mathcal{F}^{-1}\{\ldots\}$ denote the Fourier transformation and its inverse, respectively. This allows us to compute time series of LGD gravitational quantities from kinematic range-acceleration $\delta\ddot{\rho}$, with an error of only a few per cent over the frequency band above 5 CPR, equivalent to ~4,000 km and smaller in terms of spatial resolution (Ghobadi-Far et al., 2018). The limitation on the frequency band makes the LGD observations most suitable for regional applications. The transfer function by Ghobadi-Far et al. (2018), obtained from orbit and gravity simulation for the GRACE mission, can be described by an analytic equation such as:

$$Z(f) = 1.0 + 3.5^{-4} f^{-1.04}. \tag{12}$$

We validate the above transfer function using independent inter-satellite ranging data from GRACE-FO and Gravity Recovery and Interior Laboratory (GRAIL) satellites (Zuber et al., 2013). As stated earlier, the transfer function is not dependent on magnitude of gravitational signals and satellite altitude. Therefore, we can even use GRAIL satellite data and the lunar gravity field for this purpose.

We used the time series of $\delta\ddot{\rho}$ from GRACE-FO KBR and LRI data. We computed the synthetic LGD time series using the JPL L2 monthly-mean solutions to degree 96, obtained from KBR data (Yuan, 2019). Both synthetic LGD and observed $\delta\ddot{\rho}$ are computed as residual quantities referenced to the background static gravity model GGM05C. We also computed synthetic LGD from the difference between the static gravity model GOCO06s (Kvas et al., 2019) and GGM05C from degree 97 to 360. We note that the time-variable coefficients of GOCO06s representing the trend and annual variations are not used when computing LGD from this model. In the case of GRAIL, we used $\ddot{\rho}$ from the KBR sensor and computed synthetic LGD from the lunar geopotential model GL0900D to degree 900 (Konopliv et al., 2014). For the GRAIL data processing, we refer to Han (2013). Low altitude (~30 km) of GRAIL orbit during the extended mission leads to sensitivity of gravity signals to much

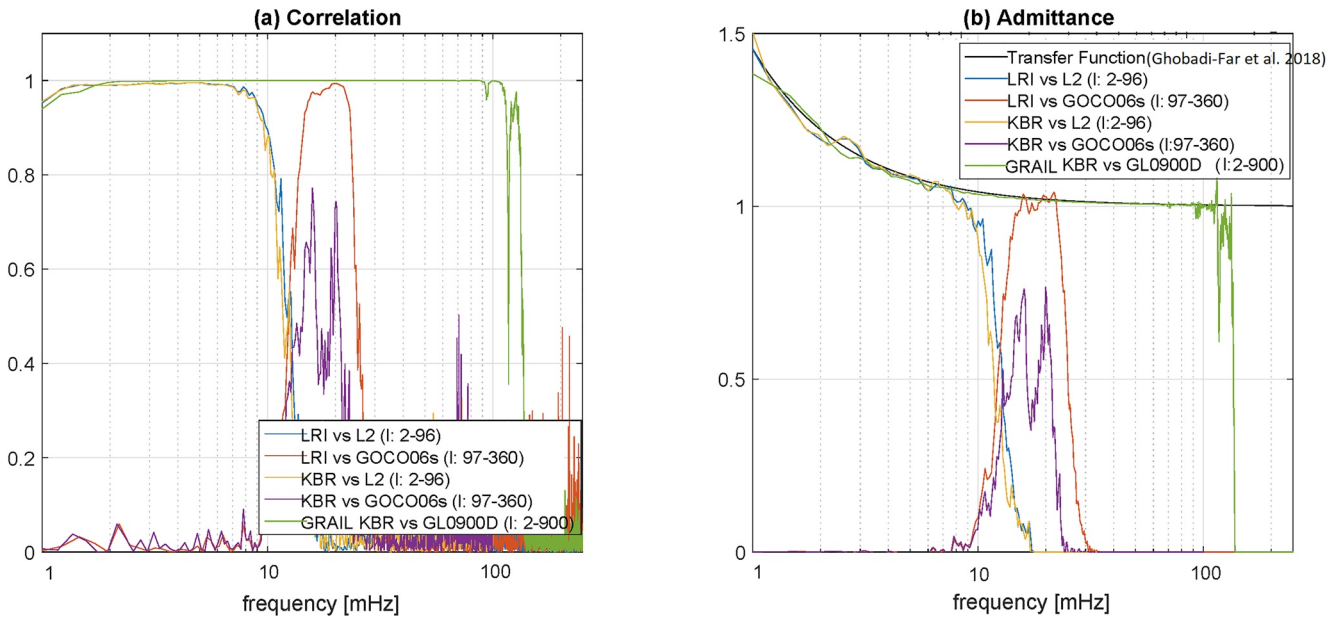

Figure 3. (a) Correlation and (b) admittance (or transfer function) spectra estimated from various pairs of inter-satellite range-acceleration measurements (GRACE-FO KBR, LRI, and GRAIL KBR) and synthetic line-of-sight gravity difference (from L2, GOCO06s, and GL0900D models). The correlation and admittance spectra found in Ghobadi-Far et al. (2018) are verified using various actual inter-satellite ranging data and to a much higher frequency, thanks to GRAIL data.

higher frequencies than those observed by GRACE-FO. Thus, the GRAIL data are particularly useful to validate the transfer function at high frequencies.

Figure 3a shows examples of the correlation spectrum estimates computed between $\delta\ddot{\rho}$ and $\delta g_{12}^{\mathrm{LOS}}$. There are three time series of $\delta\ddot{\rho}$ from GRACE-FO LRI and KBR, and GRAIL KBR, while three time series of $\delta g_{12}^{\mathrm{LOS}}$ from JPL monthly-mean L2 solution (degrees 2–96), GOCO06S (degrees 97–360), and GL0900D (degrees 2–900) models. The L2 and GOCO06s models were compared with GRACE-FO LRI and KBR, resulting in four correlation spectra, and GL0900D was compared with GRAIL KBR; therefore, there are a total of five correlation spectra. The high correlation over the frequencies below 10 mHz (60 CPR) from GRACE-FO and GRAIL data were found (blue, yellow, and green curves). Only LRI data (not KBR) were highly correlated with the static gravity model GOCO06s at higher frequencies to 25 mHz, indicating greater sensitivity of LRI data to short wavelength static gravity signals (Ghobadi-Far, Han, McCullough, et al., 2020). The correlation spectrum estimated from GRAIL data exhibits nearly perfect correlation up to 100 mHz.

Correspondingly, the admittance spectra are shown in Figure 3b. The pre-determined transfer function by Ghobadi-Far et al. (2018) obtained using GRACE synthetic orbit and gravity computation is shown for comparison. In general, the empirically calculated admittance spectra from real GRACE-FO and GRAIL data agree with the pre-determined transfer function quite well for the frequency from 1 to 10 mHz. The GRACE-FO LRI provides additional observation to the transfer function up to 25 mHz. The GRAIL data further confirms the transfer function to a much higher frequency of around 100 mHz.

Figure 4 presents the amplitude spectral density of different LGD time series determined from actual KBR and LRI measurements and from L2 TVG and GOCO06s static model, all computed as residuals with respect to the reference model GGM05C. The LRI noise and accelerometer noise from Spero (2021) in terms of LGD are also shown. KBR and LRI residuals are consistent with the L2 TVG model to frequencies below 10 mHz, indicating the dominance of TVG signals in this band. In the frequency band of 10–25 mHz, LRI residuals show gravitational anomalies consistent with the static model GOCO06s. This shows that LRI captured the residual static gravity signals not properly modeled by the reference model GGM05C (see Ghobadi-Far, Han, McCullough, et al., 2020 for more details). As such, the LRI residuals referenced to GGM05C represent low-frequency TVG as well as high-frequency (residual) static gravity signals. To demonstrate this in the spatial domain, we extracted all the GRACE-FO tracks in January 2019 passing over the eastern edge of Himalayas around the longitude of

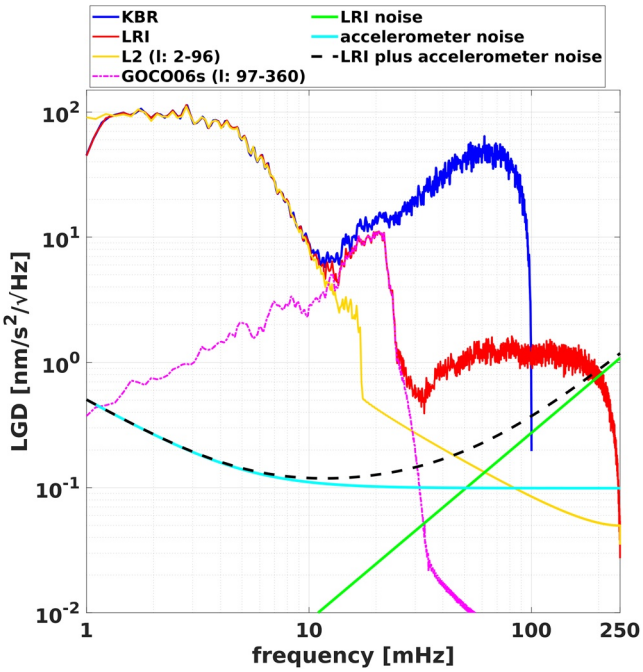

Figure 4. Amplitude spectral density of inter-satellite K-band microwave ranging and laser ranging interferometer (LRI) residuals as well as monthly-mean L2 and static gravity model GOCO06s, all represented in terms of line-of-sight gravity difference residuals referenced to GGM05C. LRI noise and GRACE Follow-On (GRACE-FO) accelerometer noise form Spero (2021) are also shown. This figure is based on the actual GRACE-FO data on 1 January 2019.

105°E and compared the observations and models in Figure 5. This figure demonstrates that by superimposing the low-resolution (degrees 2–96) TVG on high-resolution (97–360) static gravity, one can almost perfectly simulate the gravitational signals represented by the LRI residuals referenced to GGM05C. We note that the accelerometer noise shown in Figure 4 does not include the systematic errors in accelerometer measurements like errors of the thrust model used in calibration of the GRACE-FO L1B accelerometer data (see McCullough et al., 2019). Such systematic errors contribute significantly to the LRI residual error budget at high frequencies above ∼40 mHz.

4. Analysis of LRI Measurements for Sub-Monthly Surface Mass Variations

For analysis of TVG signals, we applied a high-pass filter at 1 mHz (5 CPR) frequency to GRACE-FO LRI residuals and also removed the remaining static gravity signals from LRI residuals referenced to GGM05C (originally used for release 6 data products by JPL) using GOCO06s, because GOCO06s provides the best fit results to LRI measurements among other state-of-the-art static gravity models at higher frequencies (Ghobadi-Far, Han, McCullough, et al., 2020). We present three examples of sub-monthly SMC processes to demonstrate new applications of high-precision LRI measurements based on our unique along-orbit analysis approach of TVG signals.

4.1. High-Frequency Ocean Gyre in the Argentine Basin

Located in the southwest Atlantic Ocean, the Argentine Basin is associated with complex ocean dynamics at wide-ranging spatial and temporal scales. According to satellite altimetry, some of the largest high-mesoscale variability in the world ocean occurs on the western side of the basin, in the confluence zone of the Brazil and Malvinas boundary currents (Wunsch, 2015, Figure 3.32). To the east of this zone, in the center of the basin, is a region of considerably weaker variability, which is nonetheless dominant when altimetry is filtered to reveal only large scales (>1,000 km) and temporal scales from 20 to 100 days (Fu et al., 2001). Trapped around a topographic feature called the Zapiola Rise near 45°S, 45°W is an intense anticyclonic circulation, which includes a dipole-like rotating mode of period 20–25 days and spatial scale ∼1,000 km. The mode is barotropic, which is known from ocean current measurements (Saunders & King, 1995), bottom-pressure measurements (Hughes et al., 2007), and a high-resolution ocean model (de Miranda, 1999). It is therefore in principle detectable by gravimetry, and indeed using 10-day GRACE solutions from Groupe de Recherche de Géodesie Spatiale (Lemoine et al., 2007), Han et al. (2014) and Yu et al. (2018) showed that GRACE could detect the feature. Note that although the mode is barotropic, it fails to appear in barotropic ocean models, and even in many baroclinic models, because it is evidently excited by eddy-driven vorticity supplied from the surrounding high-mesoscale ocean. Thus, only high-resolution, eddy-permitting baroclinic models are capable of simulating the ∼25-day mode (de Miranda et al., 1999; Hughes et al., 2007).

We examined the LRI residuals referenced to the long-term mean field over the Argentine Basin in January 2019. We found ten ascending and ten descending GRACE-FO tracks over the region from longitude 55°W to 45°W and compared the LGD LRI observations (LGD^{LRI}) with synthetic LGD from monthly-mean L2 solution (LGD^{L2}) of January 2019 along those tracks. Figure 6a shows the ascending ground tracks, and Figure 6b shows the corresponding LGD^{LRI} and LGD^{L2} signals, depicted by color and solid black curves, respectively. Synthetic LGD^{L2} is only a function of location (over a period of one month), while LGD^{LRI} observations represent instantaneous gravitational variability in space and time. Figure 6b clearly demonstrates how the commonly used monthly-mean L2 solutions capture the average variability over a month. The LGD^{L2} show a common positive anomaly of ∼2–3 nm/s^2 from latitude 50°S to 35°S, where the strong barotropic variability in the Argentine Basin occurs (Fu et al., 2001, also see Figure 9). The LRI observations, on the other hand, show instantaneous anomalies varying from +1 nm/s^2 on 28 January to +6 nm/s^2 on 16 January. It is seen that on 10, 11, 16, and 17 January LGD^{LRI}

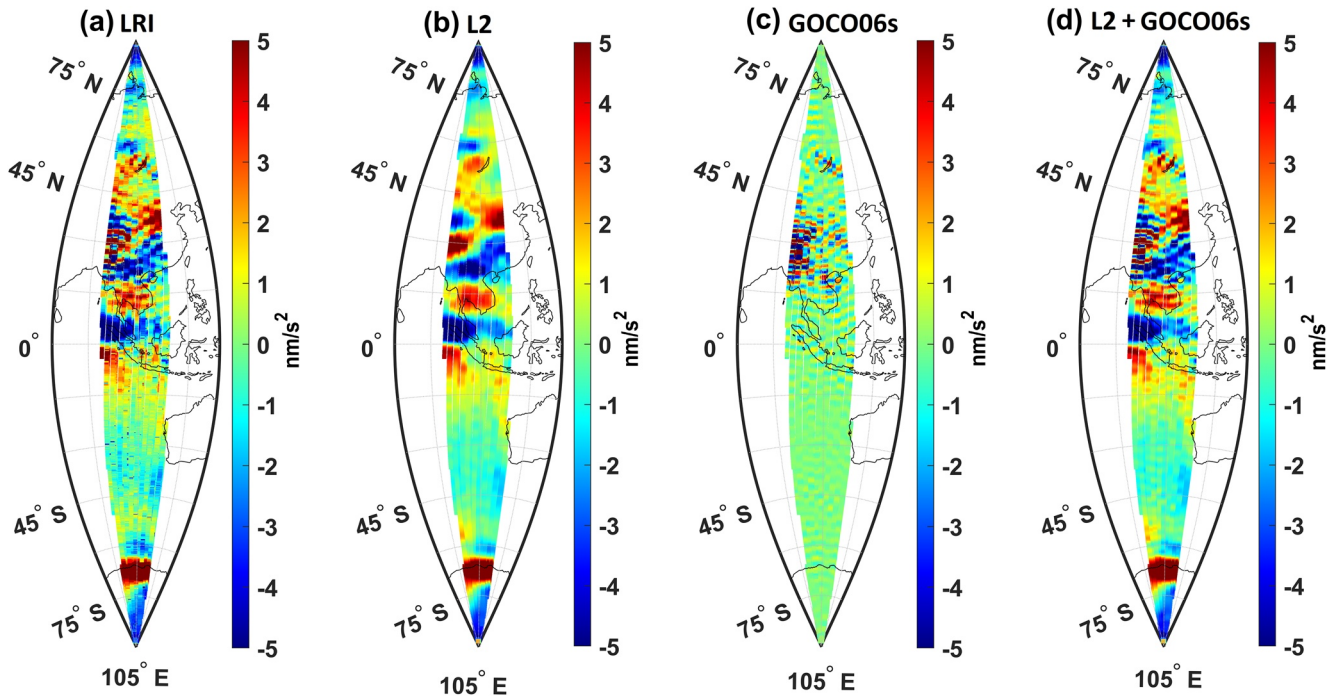

Figure 5. Spatial map of (a) LGD LRI observations, (b) synthetic line-of-sight gravity difference (LGD) from monthly-mean L2 model, (c) synthetic LGD from GOCO06s model, and (d) summation of (b and c), along the GRACE Follow-On tracks in January 2019 near longitude 105°E. All observations and models are computed as residual signals with respect to GGM05C. The laser ranging interferometer (LRI) residuals referenced to GGM05C represent low-resolution time-variable gravity and high-resolution (residual) static gravity signal (mainly over the eastern edge of Himalayas).

is larger than LGD^{L2}, while on other days the LRI anomalies are roughly equal to or smaller than L2. The same conclusion can be drawn for descending tracks shown in Figures 6c and 6d, and also for GRACE-FO tracks from longitude 45°W to 35°W (not shown). The mismatch between the instantaneous LRI measurements and L2 solutions points to the sub-monthly variability in the Argentine Basin and the fact that monthly-mean L2 solutions are not the appropriate data products for analysis of such high-frequency processes. Furthermore, the mismatch also highlights that the AOD1B RL6 model (Dobslaw et al., 2017), included in the background models to remove the sub-monthly non-tidal oceanic variability, does not adequately predict the high-frequency mass changes in the Argentine Basin. As noted above, this is to be expected in an ocean general circulation model with approximately 1° horizontal resolution that is not constrained by oceanographic in situ data.

To help explain the discrepancy between (instantaneous) LRI and (monthly-mean) L2 data, we used daily sea level anomaly (SLA) maps on a 0.25° × 0.25° grid generated from observations of multi-mission satellite altimeters (Taburet et al., 2019). Before gridding, these data had been subjected to high-frequency de-aliasing by removing sea-surface heights from a high-resolution barotropic model (Carrère et al., 2016); to avoid removing our signal of interest, we restored the dynamic ocean signals from this model, but not inverted-barometer signals since the latter do not affect gravimetry measurements. We then obtained the sub-monthly changes by subtracting the monthly-mean SLA of January 2019 from daily SLA maps, and removed the AOD1B RL6 ocean model from altimetry SLA to make them consistent with the LRI residuals. As the next step, we computed synthetic LGD from the sub-monthly SLA observations (using numerical integration described in Section 2.2.2) and added it to LGD^{L2}. The results, represented by dashed black curves in Figures 6b and 6d, show that satellite ocean altimetry data can explain the sub-monthly TVG signal in LRI measurements to a large extent, especially when there is a big difference between LRI and L2 (e.g., see the case of 16 January 2019).

The difference between instantaneous LRI residual measurements and monthly-mean L2 in terms of LGD represents fast gravitational changes at satellite altitude occurring within a month. Figure 7 shows the sub-monthly LGD^{LRI} observations, obtained after subtracting LGD^{L2}, and sub-monthly LGD computed from altimeter SLA for the ascending and descending tracks (same as Figure 6). The agreement between LRI and altimetry observations

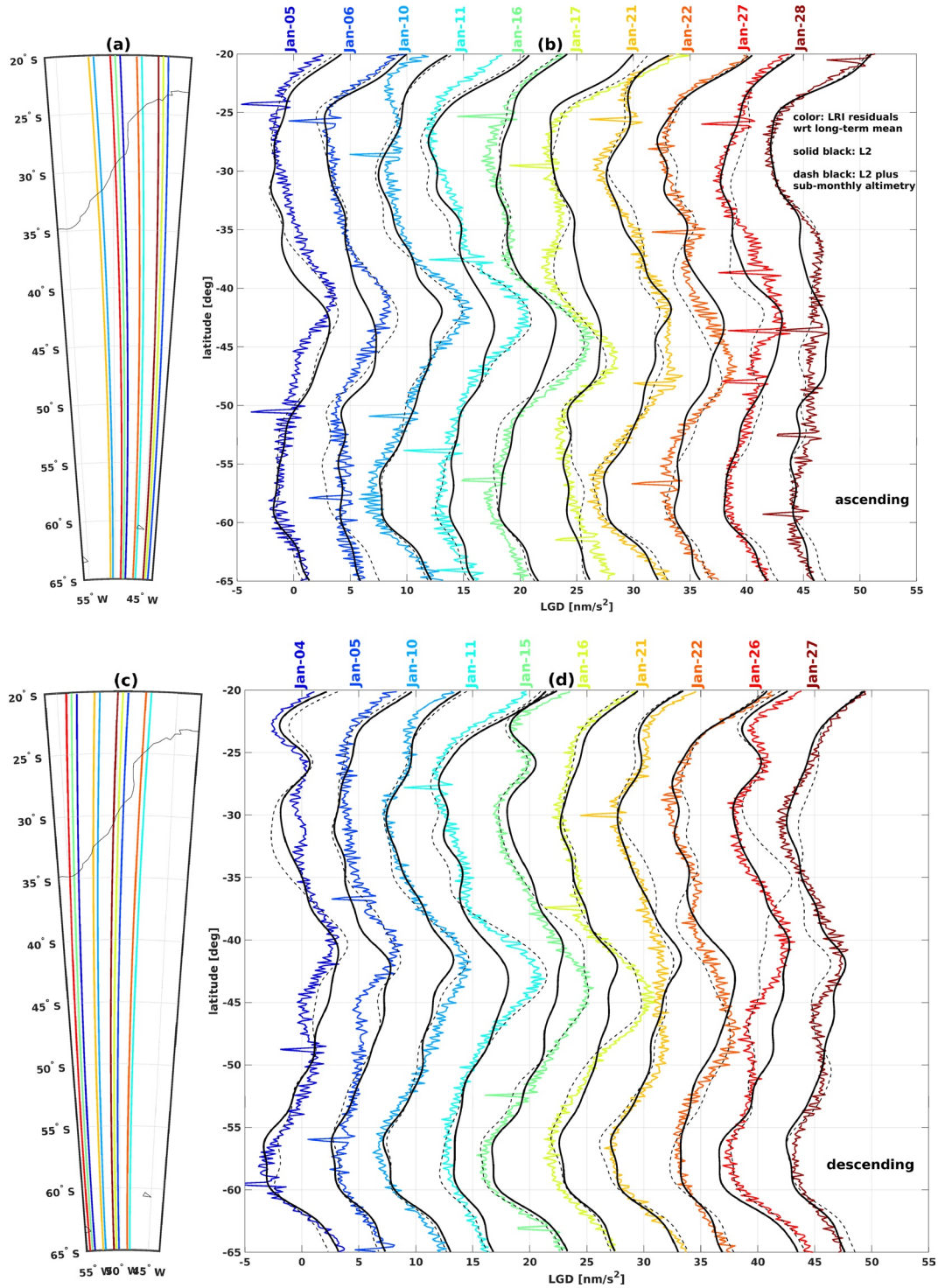

Figure 6. (a) Ascending and (c) descending ground tracks of GRACE Follow-On (GRACE-FO) in January 2019 with average longitude between 55°W and 45°W passing over the Argentine Basin. Comparison between laser ranging interferometer (LRI) measurements (color) and monthly-mean L2 (solid black), both computed as referenced to the long-term mean GOCO06s in terms of line-of-sight gravity difference, for (b) ascending and (d) descending tracks. The dashed black curves represent the monthly-mean L2 plus the sub-monthly ocean variability from satellite altimetry measurements. GRACE-FO LRI detects the high-frequency (~25 days) rotating gyre (from latitude 50°S to 35°S) in the Argentine Basin. LRI residuals along the consecutive ground tracks are offset by 5 nm/s^2.

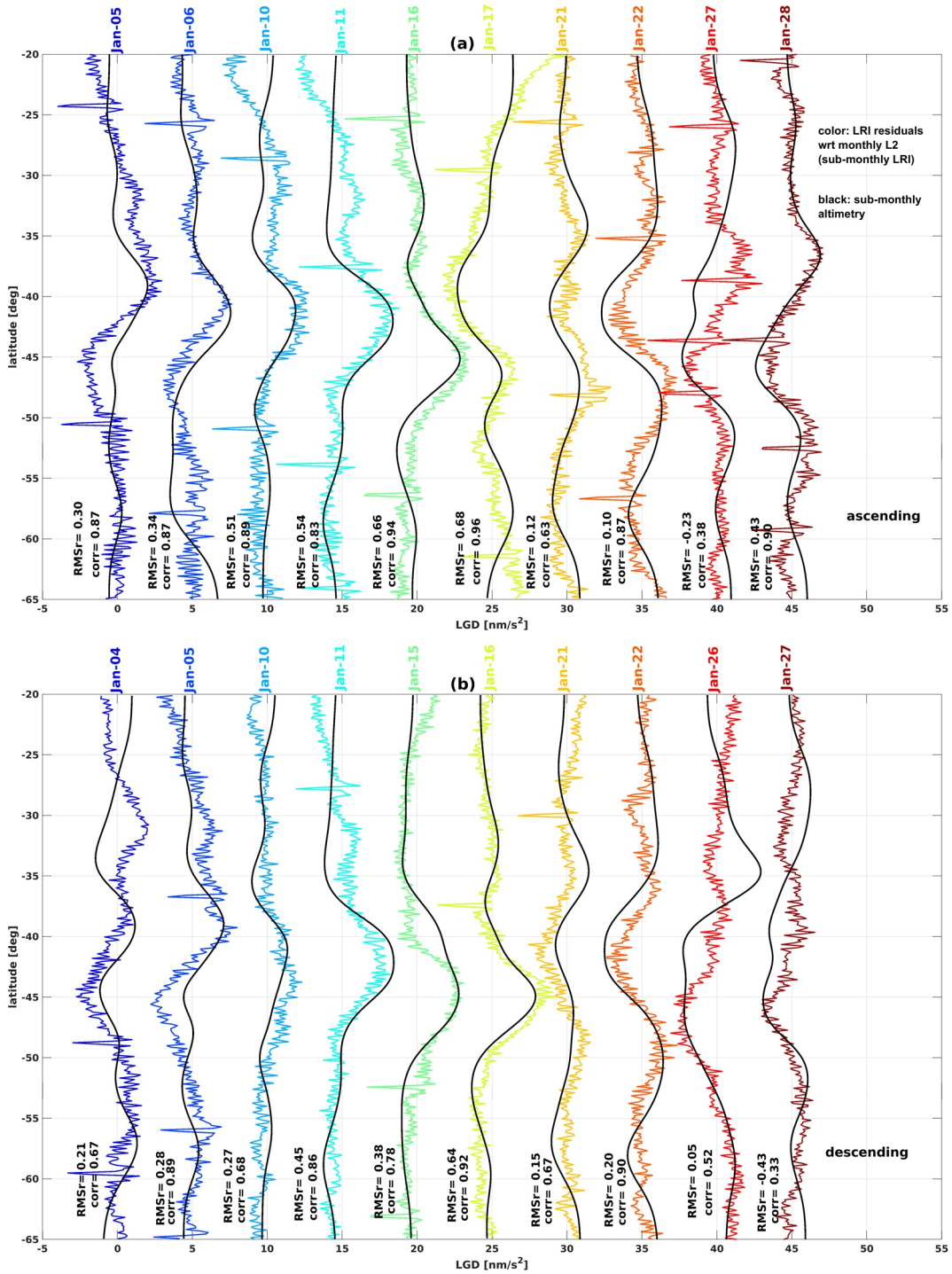

Figure 7. Comparison between observed LGD LRI anomaly referenced to the monthly-mean (i.e., sub-monthly LGD LRI) and synthetic line-of-sight gravity difference (LGD) computed from sub-monthly altimeter sea level anomalies along the GRACE Follow-On (a) ascending and (b) descending tracks in January 2019 corresponding to Figure 6. Correlation and root-mean-square reduction values for LGD data from latitude 50°S to 35°S are given.

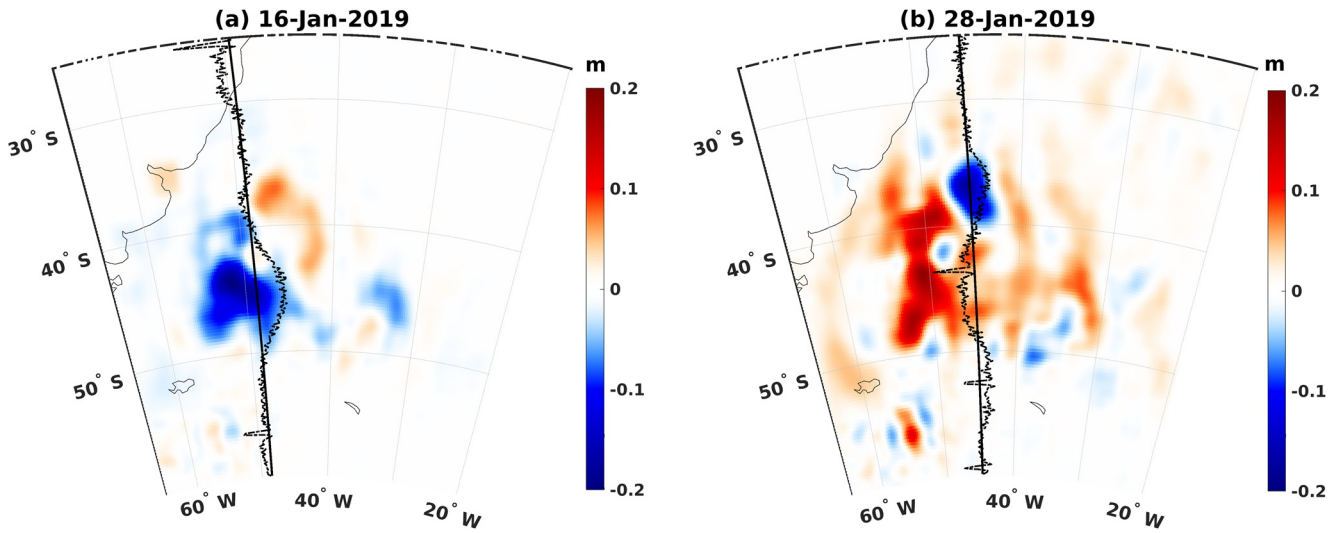

Figure 8. Examples of sub-monthly sea level anomalies from satellite altimetry observations (smoothed with a 3° × 3° window) on (a) 16 January 2019 and (b) 28 January 2019, along with the corresponding GRACE Follow-On (GRACE-FO) ascending tracks in solid black lines, reflecting the high-frequency ocean variability in the Argentine Basin (see the corresponding line-of-sight gravity difference [LGD] data along the ascending tracks on 16 and 28 January 2019 in Figure 7a). Dashed black curves represent unit-less sub-monthly LGD signal observed by the GRACE-FO laser ranging interferometer.

at sub-monthly time-scale is clearly visible. Centered at latitude ∼45°S, in the case of ascending tracks, for example, one can see a negative sub-monthly LGD anomaly on 5 January (reflecting positive SLA), a positive anomaly on 16 and 17 (reflecting negative SLA), and then again a negative anomaly on 27 and 28. The along-orbit LGD data already captured approximately 20–25 days of periodic changes in SLA.

Figure 8 shows examples of daily SLA maps on January 16 and 28 computed with respect to the monthly-mean and the GRACE-FO ascending tracks for each day. This figure illustrates how the transition of SLA from negative to positive centered at latitude ∼45°S within one month changed the LGD LRI measurements seen in Figure 7. We also computed the cross-correlation between the sub-monthly LGD LRI and SLA from latitude ∼50°S to ∼35°S as well as the RMS reduction in LRI when subtracted by SLA data (see Figure 7). The cross-correlation and RMS reduction is as high as ∼0.9 and ∼0.6, respectively. There are discrepancies of a couple of nm/s^2 between GRACE-FO LRI measurements and altimeter data for different times and locations. It may be caused by altimeter gridding and interpolation errors (the procedures depend on temporal correlation scales that may not be accurate) as well as baroclinic sea level variability not accounted for in the gravity computation from altimeter SLA.

4.2. Ocean Mass Variability in the Gulf of Carpentaria

The GoC is a large shallow sea in northern Australia which shows large seasonal (Tregoning et al., 2008) as well as high-frequency non-tidal variability (e.g., see RMS variability of ocean model outputs in Schindelegger et al., 2021). The AOD1B models are constantly being improved to better reproduce the sub-monthly variability in GoC in order to reduce the aliasing of high-frequency signals into the monthly-mean solutions. An intermediate (test) version of a new AOD1B model called v71 was recently developed at GFZ to be used as a background model in the next release of L2 solutions (Shihora & Dobslaw, 2021). In the following, we show how the LRI measurements can be employed to validate the test AOD1B model with the example in GoC. We reiterate that the AOD1B RL6 model (Dobslaw et al., 2017) was used in the background models to compute the LRI residuals employed in this article.

We examined the LRI residuals along the descending GRACE-FO tracks over GoC from 23 January 2019 to 7 February 2019. During this period, a low-pressure system brought unprecedented rainfall and flooding to north-eastern part of Australia, mainly in Queensland (Australian Bureau of Meteorology, 2019). The strong surface winds associated with this weather pattern also caused substantial oceanic variability in GoC. The six

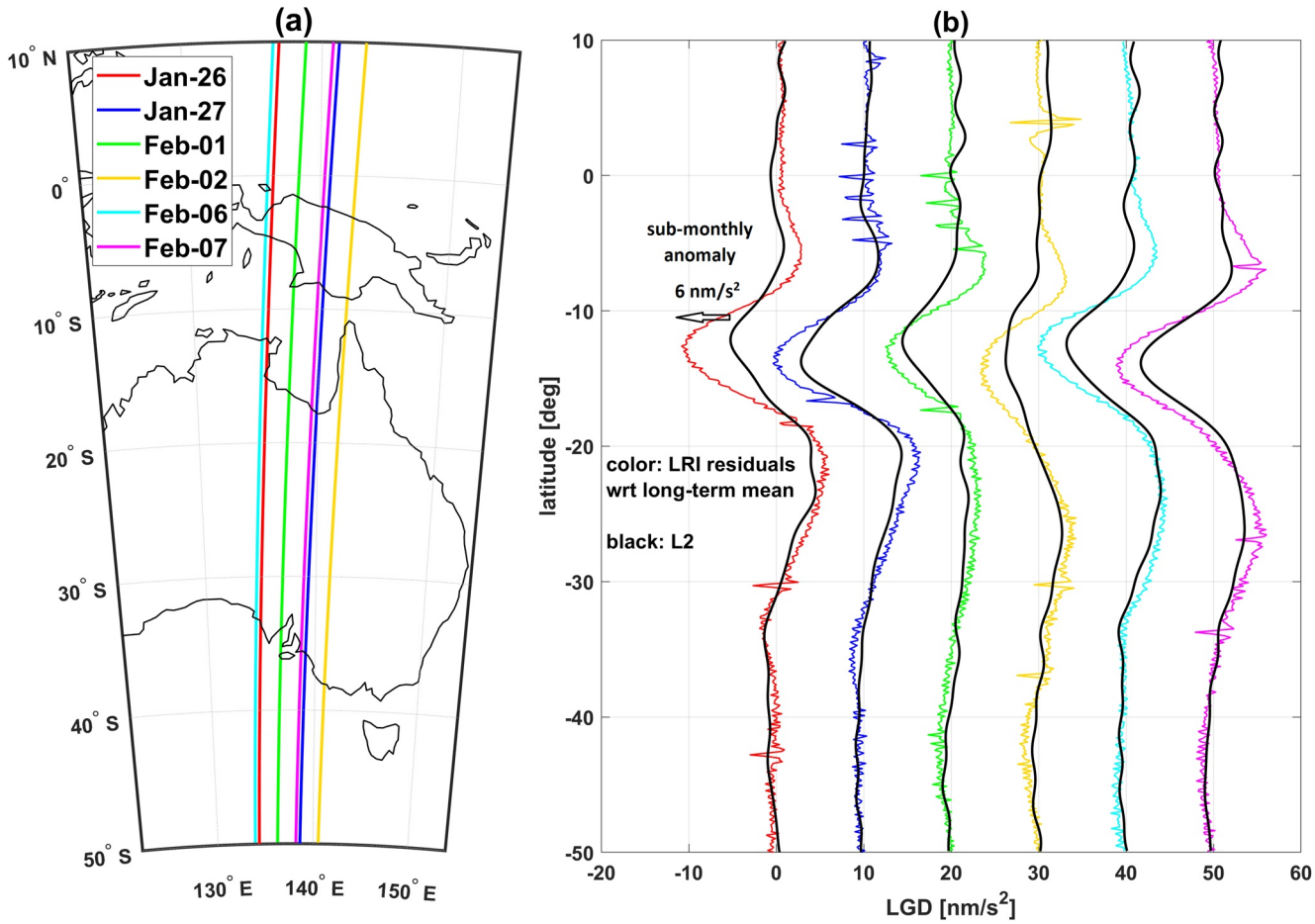

Figure 9. (a) GRACE Follow-On descending tracks near the Gulf of Carpentaria between 23 January 2019 and 7 February 2019, when a low-pressure system generated large oceanic mass variability in this region. (b) Comparison between LGD LRI observations and synthetic line-of-sight gravity difference (LGD) computed from monthly-mean L2 solutions, both computed with respect to the long-term mean GOCO06s. The difference between the color and black curves represents the sub-monthly change not captured by L2 solutions and is as large as 6 nm/s^2.

descending tracks found over this period are shown in Figure 9a. LGD^{LRI} residuals as well as LGD^{L2} form January and February 2019 solutions, both referenced to GOCO06s, are shown in Figure 9b. Monthly-mean L2 is consistently smaller (in terms of absolute value) than the instantaneous LRI; the difference (i.e., sub-monthly change) is as large as 6 nm/s^2 on 26 January. This indicates that the AOD1B RL6 model underestimates the rapid ocean mass variability in GoC over this period, resulting in large sub-monthly LRI residuals.

We removed LGD^{L2} from LRI residuals to focus on sub-monthly LGD^{LRI}, reflecting mainly the high-frequency oceanic variability not properly captured by the AOD1B RL6 model (see Figure 10). We computed synthetic LGD along the GRACE-FO descending tracks from spherical harmonic coefficients of AOD1B RL6 (3-hourly) and v71 (hourly) using the spherical harmonic expansion described in Section 2.1. The difference between the two models, representing the AOD1B model update by v71, is shown in black in Figure 10. If the AOD1B update (v71 – RL6) is positively correlated with the sub-monthly (instantaneous) LRI residuals, it means the test model v71 improves the modeling of high-frequency variability in GoC against RL6. The positive cross-correlations of ~0.8 and higher reported in Figure 10, computed for data from latitude 20°S to 0°, show that indeed this is the case. Similar results were obtained based on the ascending tracks (not shown). The improvement in v71 ocean mass change computation in GoC is likely due to inclusion of the self-attraction and loading effect into the MPIOM general ocean circulation model. Given the basin is resonant on the period of several days, the self-attraction and loading effect will be significant (Dobslaw et al., 2021; Shihora & Dobslaw, 2021). The anomaly

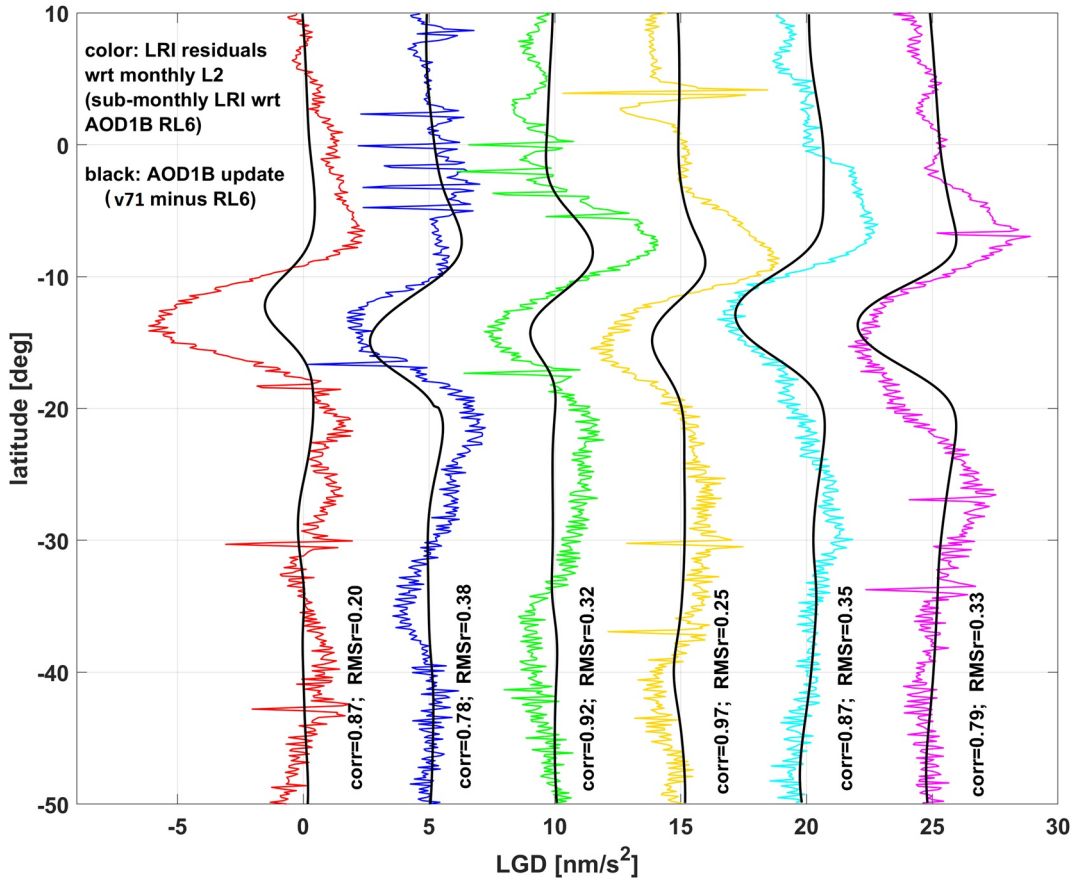

Figure 10. Comparison between observed sub-monthly line-of-sight gravity difference (LGD) LRI (N.B. it is referenced to AOD1B RL6 model) and synthetic LGD from the difference between (3-hourly) RL6 and (hourly) v71 AOD1B models along the descending tracks shown in Figure 9a. Along-orbit laser ranging interferometer (LRI) analysis reveals the significant improvement by AOD1B v71 test model for this experiment. This is likely due to inclusion of the self-attraction and loading effect in the ocean mass change computation.

in sub-monthly LRI on 7 February (magenta) from 23°S to 15°S, which is extended south and not in agreement with the AOD1B update, is caused by the flood water on land.

The along-orbit analysis of LRI residuals presented here aims at the validation of AOD1B models at a specific location and time. As an alternative approach, one can obtain global comparison of LRI residuals with respect to different AOD1B models over many years and compare them to assess the improvement by newer models. For example, see the comparison of AOD1B RL5 and RL6 using KBR residuals (obtained after low pass filtering to suppress the KBR noise at high frequencies) in Dobslaw et al. (2017). Both approaches are complementary and provide useful information about the performance of AOD1B models from different aspects. While the former is more suitable for model evaluation associated with a specific phenomenon like a tropical cyclone, the latter helps to delineate regions where the new model improves (or worsens) the high-frequency mass variability averaged over many years.

4.3. Surface Water Transport in the Amazon Basin

As a hydrological example of sub-monthly mass change, we focus on surface water including water in floodplains and river channels in the Amazon. In high water periods like April, surface water plays a significant role in the Amazon water budget and contributes to as much as ∼50% of the total water storage (Han et al., 2009). Compared to the soil moisture, which is spatially disperse and varies at broad spatial scales, surface water is spatially localized (e.g., Han et al., 2009; Kim et al., 2009). Moreover, surface water storage changes faster than soil moisture

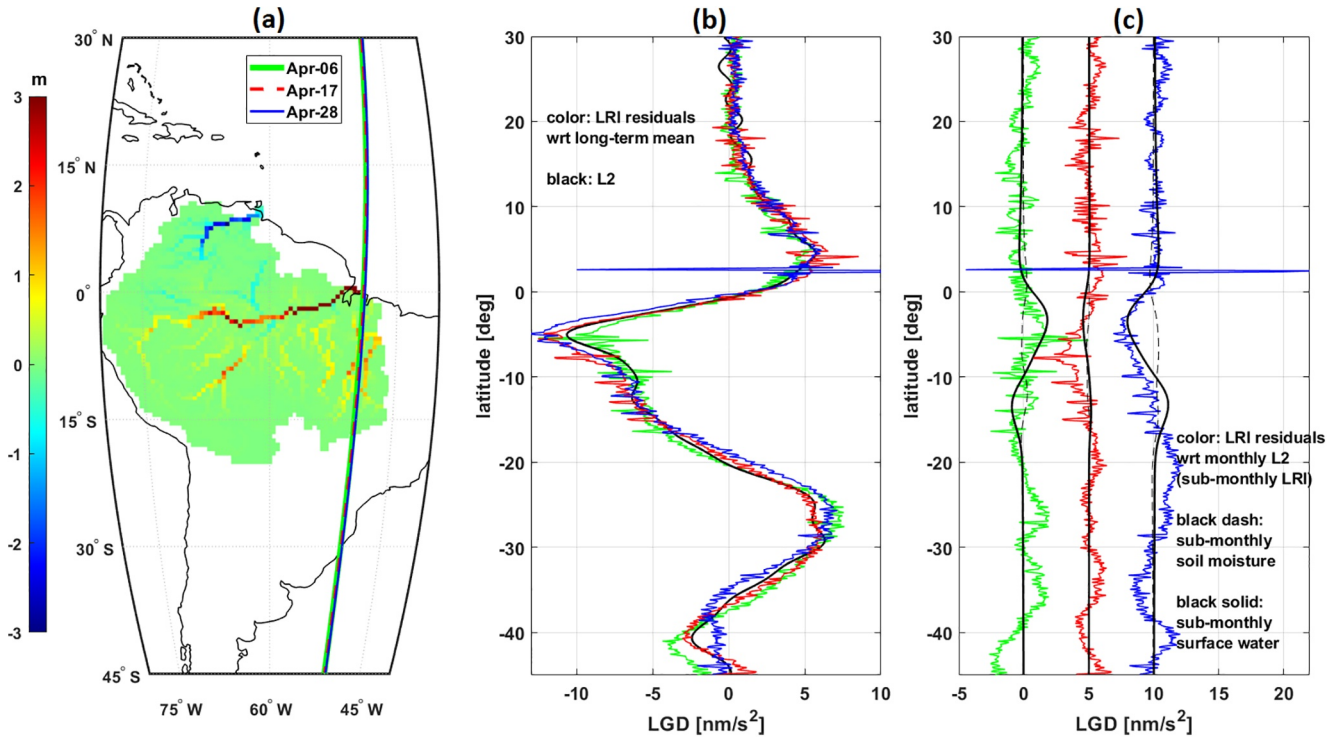

Figure 11. (a) Monthly-mean surface water storage in April 2020 simulated from GLDAS/NOAH runoff with the effective routing velocity of 0.1 m/s in the Amazon, Orinoco, and Tocantins Basins, along with GRACE Follow-On descending tracks (almost repeat passes) in April 2020 near longitude 50°W on 6, 17, and 28 April 2020. (b) Comparison between laser ranging interferometer (LRI) data and monthly-mean L2 in terms of line-of-sight gravity difference (LGD) change referenced to a long-term mean. (c) Sub-monthly LGD changes measured from LRI (colors) and comparison to sub-monthly soil moisture (dashed black) and sub-monthly surface water storage (solid black). Note the agreement between LGD measurements and sub-monthly surface water storage model (not soil moisture model) from latitude 10°S to 0° on 6 and 28 April 2020.

storage with larger amplitude variation. We examined the LRI data for such high-frequency hydrological mass variation caused by surface water storage.

Instead of extracting GRACE-FO tracks within a longitudinal band as in the case of previous oceanic examples, we searched for the GRACE-FO tracks passing almost over the same location (the so-called repeat tracks) in April 2020. GRACE-FO satellites completed 167 orbital revolutions in 11 days in April 2020. Figure 11a shows three descending tracks at the longitude of 50°W passing over the Tocantins River and near the Amazon mouth on 6, 17, and 28 April 2020. The comparison between LRI and L2, both computed as residuals referenced to GOCO06s, shown in Figure 11b, indicates that instantaneous LRI measurements near latitude 5°S are smaller in early April and larger in late April than the monthly-mean L2. Figure 11c illustrates the sub-monthly LRI residuals on different days. The sub-monthly LGD variability is less extensive covering only ~10° in latitude (from latitude 10°S to 0°) than the LGD variability with respect to the long-term mean (see anomaly from latitude 20°S to 0° in Figure 11b), likely indicating the localized mass anomalies. The positive and negative anomaly on 6 and 28 April indicates mass deficit and excess relative to the monthly-mean total water storage, respectively.

To explore the cause of sub-monthly LRI variability, we obtained soil moisture from the GLDAS/NOAH model (Rodell et al., 2004) in the Amazon, Orinoco and Tocantins Basins, and computed its daily variability with respect to the monthly-mean of April 2020. Furthermore, we simulated surface water storage changes by routing the GLDAS/NOAH runoff using the Total Runoff Integrating Pathways (TRIP) river network (Oki et al., 1999) and the effective velocity of 0.1 m/s. A small velocity like 0.1 m/s better fits the GRACE inter-satellite ranging data in April (Han et al., 2009). Like soil moisture, we computed the daily change in surface water referenced to the April 2020 monthly-mean. Figure 12 shows that surface water varies substantially from ~−0.5 m to ~+0.5 m within a month over the major Amazon and Tocantins River tributaries. In contrast, the soil moisture sub-monthly changes are much smaller (~0.05 m) and more spatially disperse. We computed the synthetic LGD from

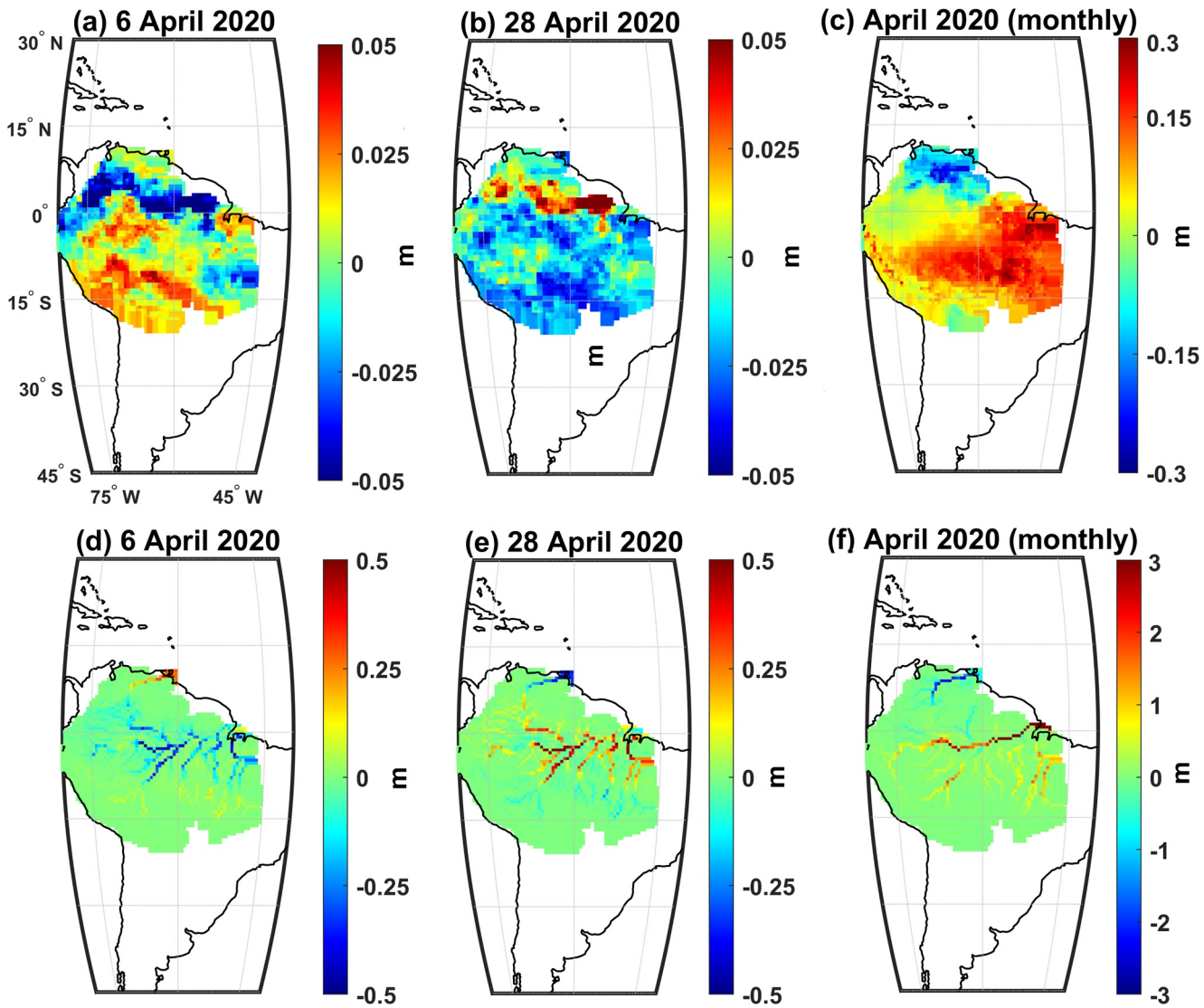

Figure 12. Sub-monthly soil moisture on (a) 6 April 2020 and (b) 28 April 2020, as well as (c) the monthly-mean soil moisture in April 2020 from GLDAS/NOAH in the Amazon, Orinoco, and Tocantins Basins. Sub-monthly surface water storage on (d) 6 April 2020 and (e) 28 April 2020, as well as (f) the monthly-mean surface water storage in April 2020. Surface water storage was simulated by routing the GLDAS/NOAH runoff with a constant velocity of 0.1 m/s. The daily anomaly of surface water storage with respect to the monthly-mean is by far larger and more localized than that of soil moisture storage.

sub-monthly soil moisture and surface water grids (using numerical integration approach) and compared them with the sub-monthly LRI measurements in Figure 11c. The surface water is capable of successfully explaining LRI sub-monthly anomaly from latitude − 10°S to 0° in early and late April. However, the simulated surface water does not reproduce the LRI anomaly from latitude − 15°S to − 5°S on 17 April, possibly indicating, among others, the limitation of constant velocity and error in the model runoff.

To provide additional context for our GRACE-FO results, and as an independent measure of the timing of the maximum water storage for sites near the GRACE-FO ground tracks, we examined continuous GPS (cGPS) observations of vertical position as a function of time from late 2019 to late 2020. For this example, we selected cGPS sites adjacent to the Tocantins River and the outflow of this tributary near the Amazon River mouth (see Figure S1 in Supporting Information). As inferred from the vertical loading history cGPS data, the maximum subsidence occurs at sequentially later times for sites from higher elevations that are closer to the river catchment (TOPL) progressing to (MABA) to a near-coastal site (BELE; Figure S2). The GRACE-FO LRI LGD data from April (Figure 11b) illustrate slices in time when water loading increased to a maximum near the cGPS site MABA (latitude 5.3°S) in late April.

5. Summary and Outlook

A new approach of "along-orbit" gravity data analysis, in contrast to spatial data analysis ("monthly-mean" gravity field inversion), was explained and demonstrated with three different examples of sub-monthly mass variations. This method fully exploits the superb sensitivity of GRACE-FO LRI data and brings advantages to examine instantaneous TVG changes. We presented a new gravimetric data product of LGD time series along the satellite orbit estimated from LRI measurements. LGD is a measurement of in situ, relative gravity variation at orbital altitude and at a given time, and it can be determined from LRI data through the spectral domain transfer function (Ghobadi-Far, Han, McCullough, et al., 2020). We validated the LGD transfer function developed with GRACE orbit and gravity simulation by Ghobadi-Far et al. (2018) using new GRACE-FO KBR and LRI, as well as GRAIL inter-satellite tracking data to address the robustness of this approach across a wide range of frequencies.

We presented how to synthesize LGD time series from TVG L2 fields and SMC grids of geophysical models to evaluate the uncertainty of the models by direct comparison to in situ LGD LRI measurements. This has several merits beyond the use of monthly-mean L2 and L3 data products. The model assessment against the L2/L3 data is difficult owing to various levels of post-processing applied to the data, resulting in spatially smoothed and scaled information. In addition, strictly speaking, the L2/L3 data are not precisely the monthly-mean due to inhomogeneous ground track coverage and transient (non-stationary) mass change signals. The regularized solutions at different time-scales including daily (e.g., Mayer-Gürr et al., 2018), 5-day (Save et al., 2020) and 10-day (Lemoine et al., 2007) solutions are alternatives to advance the use of gravity data for short-term mass change processes. However, these regularized results rely on constraints and regularization in the solution process, which have the potential to introduce biases in the estimate. On the other hand, the model assessment against the LGD observations is straightforward and unique (unlike inversion) and bypasses all complications associated with spatial filtering, smoothing, and more importantly it is free of temporal aliasing error, as we demonstrated in this study with the examples of high-frequency oceanic and terrestrial water mass changes.

Extending the application of LGD further, the LGD observations are suitable for model calibration and data assimilation. In particular, the instantaneous gravity perturbation data like LGD (as opposed to the current practice of monthly-mean L2/L3 data assimilation) can be used for hydrology data assimilation at higher temporal resolution (like daily) by updating the model state parameters frequently with precise timing and location of the LRI measurements along with their error information.

The monthly-mean L2 and L3 data products from GRACE/GRACE-FO have proven to be effective for monitoring and studying mass change signals with mainly seasonal to interannual variability. The methodology presented in this study is a way of scientifically utilizing high-precision LRI data to extract short-term (sub-monthly) mass change signals. Thus, it broadens the scope of geophysical applications that can be addressed by GRACE/GRACE-FO satellites data. The LGD time series (computed from LRI) can be introduced as a new gravity data product for the GRACE-FO mission.

Acknowledgments
This work was funded by the University of Newcastle to support NASA's GRACE and GRACE Follow-On projects as an international science team member and by Australian Research Council Discovery Program (DP160104095, DP170100224). Science team funding was provided by NASA (GRACERFO19-0010) to Jeanne Sauber. A portion of this research was carried out at the Jet Propulsion Laboratory, California Institute of Technology, under a contract with the National Aeronautics and Space Administration (80NM0018D0004). The work towards AOD1B RL07 is supported by the German Research Foundation (DO 1311/4-1). Open access publishing facilitated by The University of Newcastle, as part of the Wiley – The University of Newcastle agreement via the Council of Australian University Librarians.

Data Availability Statement

The GRACE-FO Level-1B and Level-2 data used in this study are publicly available at https://podaac.jpl.nasa.gov/GRACE. Earth static gravity field models are available at http://icgem.gfz-potsdam.de/tom_longtime. TRIP river channel was obtained from http://hydro.iis.u-tokyo.ac.jp/~taikan/TRIPDATA/TRIPDATA.html. Satellite altimeter data were obtained from the Copernicus Marine Service at https://marine.copernicus.eu. The altimeter de-aliasing model data are available from https://www.aviso.altimetry.fr.

References

Abich, K., Abramovici, A., Amparan, B., Baatzsch, A., Okihiro, B. B., Barr, D. C., et al. (2019). In-orbit performance of the GRACE Follow-On laser ranging interferometer. *Physical Review Letters*, *123*(3), 031101. https://doi.org/10.1103/PhysRevLett.123.031101

Allgeyer, S., Tregoning, P., McQueen, H., McClusky, S. C., Potter, E.-K., Pfeffer, J., et-al. (2022). ANU GRACE Data Analysis: Orbit modeling, regularization and inter-satellite range acceleration observations. *Journal of Geophysical Research: Solid Earth*. https://doi.org/10.1029/2021jb022489

Australian Bureau of Meteorology. (2019). *Special climate statement 69—An extended period of heavy rainfall and flooding in tropical Queensland. Report*.

Carrère, L., Faugère, Y., & Ablain, M. (2016). Major improvement of altimetry sea level estimations using pressure-derived corrections based on ERA-Interim atmospheric reanalysis. *Ocean Science*, *12*, 825–842. https://doi.org/10.5194/os-12-825-2016

de Miranda, A. P., Barnier, B., & Dewar, W. K. (1999). On the dynamics of the Zapiola anticyclone. *Journal of Geophysical Research*, *104*, 21137–21149. https://doi.org/10.1029/1999jc900042

Dobslaw, H., Bergmann-Wolf, I., Dill, R., Poropat, L., Thomas, M., Dahle, C., et al. (2017). A new high-resolution model of non-tidal atmosphere and ocean mass variability for de-aliasing of satellite gravity observations: AOD1B RL06. *Geophysical Journal International*, *211*(1), 263–269. https://doi.org/10.1093/gji/ggx302

Dobslaw, H., Shihora, L., & Sulzbach, R. (2021) High-Frequency Sea-Level Variations driven by Self-Attraction and Loading from Atmospheric Surface Pressure at the Continents, EGU General Assembly 2021, online, 19–30 Apr 2021, EGU21-12970. https://doi.org/10.5194/egusphere-egu21-12970

Fahnestock, E., Wiese, D. N., Yuan, D. N., McCullough, C. M., Landerer, F. W., & Webb, F. (2019). GRACE-FO Gravity Field Results from JPL to Date, and Their Continuity with GRACE Results. AGU Fall Meeting, 9–13 December 2019, San Francisco, USA.

Farrell, W. E. (1972). Deformation of the Earth by surface loads. *Reviews of Geophysics*, *10*(3), 761–797. https://doi.org/10.1029/RG010i003p00761

Flechtner, F., Neumayer, K. H., Dahle, C., Dobslaw, H., Fagiolini, E., Raimondo, J. C., & Güntner, A. (2016). What can be expected from the GRACE-FO laser ranging interferometer for Earth science applications? In *Remote sensing and water resources* (pp. 263–280). Cham: Springer. https://doi.org/10.1007/978-3-319-32449-4_11

Fu, L. L., Cheng, B., & Qiu, B. (2001). Twenty fifth-day period large-scale oscillations in the Argentine Basin revealed by the TOPEX/Poseidon altimeter. *Journal of Physical Oceanography*, *31*(2), 506–517.

Ghobadi-Far, K., Han, S. C., Allgeyer, S., Tregoning, P., Sauber, J., Behzadpour, S., et al. (2020). GRACE gravitational measurements of tsunamis after the 2004, 2010, and 2011 great earthquakes. *Journal of Geodesy*, *94*(7), 1–9. https://doi.org/10.1007/s00190-020-01395-3

Ghobadi-Far, K., Han, S. C., McCullough, C. M., Wiese, D. N., Yuan, D. N., Landerer, F. W., et al. (2020). GRACE Follow-On laser ranging interferometer measurements uniquely distinguish short-wavelength gravitational perturbations. *Geophysical Research Letters*, *47*(16), e2020GL089445. https://doi.org/10.1029/2020GL089445

Ghobadi-Far, K., Han, S. C., Sauber, J., Lemoine, F., Behzadpour, S., Mayer-Gürr, T., et al. (2019). Gravitational changes of the Earth's free oscillation from earthquakes: Theory and feasibility study using GRACE inter-satellite tracking. *Journal of Geophysical Research: Solid Earth*, *124*(7), 7483–7503. https://doi.org/10.1029/2019JB017530

Ghobadi-Far, K., Han, S. C., Weller, S., Loomis, B. D., Luthcke, S. B., Mayer-Gürr, T., & Behzadpour, S. (2018). A transfer function between line-of-sight gravity difference and GRACE inter-satellite ranging data and an application to hydrological surface mass variation. *Journal of Geophysical Research: Solid Earth*, *123*(10), 9186–9201. https://doi.org/10.1029/2018JB016088

Han, S. C. (2013). Determination and localized analysis of inter-satellite line of sight gravity difference: Results from the GRAIL primary mission. *Journal of Geophysical Research: Planets*, *118*(11), 2323–2337.

Han, S. C., Jekeli, C., & Shum, C. K. (2004). Time-variable aliasing effects of ocean tides, atmosphere, and continental water mass on monthly mean GRACE gravity field. *Journal of Geophysical Research: Solid Earth*, *109*(B4). https://doi.org/10.1029/2003JB002501

Han, S. C., Kim, H., Yeo, I. Y., Yeh, P., Oki, T., Seo, K. W., et al. (2009). Dynamics of surface water storage in the Amazon inferred from measurements of inter-satellite distance change. *Geophysical Research Letters*, *36*, L09403. https://doi.org/10.1029/2009GL037910

Han, S.-C., Ray, R., & Hughes, C. (2014). *High-frequency (20–60 days) ocean mass variation over the Argentine Basin observed from GRACE, a paper presented at the GRACE Science Team Meeting*. Potsdam, Germany. Retrieved from https://www.gfz-potsdam.de/en/section/global-geomonitoring-and-gravity-field/projects/gravity-recovery-and-climate-experiment-follow-on-grace-fo-mission/gstm/gstm-2014/

Heiskanen, W. A., & Moritz, H. (1967). *Physical geodesy*. San Francisco: Freeman and Company.

Hughes, C. W., Stepanov, V. N., Fu, L.-L., Barnier, B., & Hargreaves, G. W. (2007). Three forms of variability in Argentine Basin ocean bottom pressure. *Journal of Geophysical Research*, *112*, C01011. https://doi.org/10.1029/2006JC003679

Kang, K., & Bender, P. L. (2021). Improved measurements of short-period mass variations with future Earth gravity missions. *Journal of Geophysical Research: Solid Earth*, *126*(1), e2020JB020720. https://doi.org/10.1029/2020JB020720

Kim, H., Yeh, P. J. F., Oki, T., & Kanae, S. (2009). Role of rivers in the seasonal variations of terrestrial water storage over global basins. *Geophysical Research Letters*, *36*, L17402. https://doi.org/10.1029/2009GL039006

Konopliv, A. S., Park, R. S., Yuan, D. N., Asmar, S. W., Watkins, M. M., Williams, J. G., et al. (2014). High-resolution lunar gravity fields from the GRAIL primary and extended missions. *Geophysical Research Letters*, *41*(5), 1452–1458. https://doi.org/10.1002/2013GL059066

Koop, R. (1993). *Global gravity field modeling using satellite gravity gradiometry. Tech. Rep. New Series* (Vol. 38). Delft: The Netherlands Geodetic Commission.

Kvas, A., Mayer-Gürr, T., Krauss, S., Brockmann, J.-M., Schubert, T., Schuh, W.-D., et al. (2019). *The satellite-only gravity field model GOCO06s*. GFZ Data Services. https://doi.org/10.5880/ICGEM.2019.002

Landerer, F. W., Flechtner, F. M., Save, H., Webb, F. H., Bandikova, T., Bertiger, W. I., et al. (2020). Extending the global mass change data record: GRACE Follow-On instrument and science data performance. *Geophysical Research Letters*, *47*(12), e2020GL088306. https://doi.org/10.1029/2020GL088306

Lemoine, J. M., Bruinsma, S., Loyer, S., Biancale, R., Marty, J. C., Perosanz, F., & Balmino, G. (2007). Temporal gravity field models inferred from GRACE data. *Advances in Space Research*, *39*, 1620–1629. https://doi.org/10.1016/j.asr.2007.03.062

Mayer-Gürr, T., Behzadpur, S., Ellmer, M., Kvas, A., Klinger, B., Strasser, S., & Zehentner, N. (2018). *ITSG-Grace2018—Monthly, daily and static gravity field solutions from GRACE*. GFZ Data Services. https://doi.org/10.5880/ICGEM.2018.003

McCullough, C. M., Harvey, N., Save, H., & Bandikova, T. (2019). *Description of calibrated GRACE-FO Accelerometer Data Products (ACT), Jet Propulsion Laboratory*. California, USA: California 402 Institute of Technology.

Oki, T., Nishimura, T., & Dirmeyer, P. (1999). Assessment of annual runoff from land surface models using Total Runoff Integrating Pathways (TRIP). *Journal of the Meteorological Society of Japan. Series II*, *77*(1B), 235–255. https://doi.org/10.2151/jmsj1965.77.1B_235

Ries, J., Bettadpur, S., Eanes, R., Kang, Z., Ko, U. D., McCullough, C., et al. (2016). The development and evaluation of the global gravity model GGM05. Technical Memorandum CSR-TM-16-01, Center for Space Research of University of Texas. Retrieved from https://repositories.lib.utexas.edu/handle/2152/74341

Rodell, M., Houser, P. R., Jambor, U. E. A., Gottschalck, J., Mitchell, K., Meng, C. J., et al. (2004). The global land data assimilation system. *Bulletin of the American Meteorological Society*, *85*(3), 381–394. https://doi.org/10.1175/BAMS-85-3-381

Rummel, R. (1979). Determination of short-wavelength components of the gravity field from satellite-to-satellite tracking or satellite gradiometry. *Manuscripta Geodaetica*, *4*(2), 107–148.

Saunders, P. M., & King, B. A. (1995). Bottom current derived from a shipborne ADCP on WOCE cruise A11 in the South Atlantic. *Journal of Physical Oceanography*, *25*, 329–347.

Save, H., Sun, A. Y., Scanlon, B. R., & Rateb, A. (2020). *Preliminary results from GRACE/GRACE-FO 5-day mascon solutions from CSR*. American Geophysical Union Fall Meeting.

Schindelegger, M., Harker, A. A., Ponte, R. M., Dobslaw, H., & Salstein, D. A. (2021). Convergence of daily GRACE solutions and models of sub-monthly ocean bottom pressure variability. *Journal of Geophysical Research: Oceans*, *126*(2), e2020JC017031.

Sheard, B. S., Heinzel, G., Danzmann, K., Shaddock, D. A., Klipstein, W. M., & Folkner, W. M. (2012). Inter-satellite laser ranging instrument for the GRACE Follow-On mission. *Journal of Geodesy*, *86*(12), 1083–1095. https://doi.org/10.1007/s00190-012-0566-3

Shihora, L., & Dobslaw, H. (2021). Towards AOD1B RL07, EGU General Assembly 2021, online, 19–30 April 2021. https://doi.org/10.5194/egusphere-egu21-1981

Spero, R. (2021). Point-mass sensitivity of gravimetric satellites. *Advances in Space Research*, *67*(5), 1656–1664. https://doi.org/10.1016/j.asr.2020.12.019

Taburet, G., Sanchez-Roman, A., Ballarotta, M., Pujol, M. I., Legeais, J. F., Fournier, F., et al. (2019). DUACS DT2018: 25 yr of reprocessed sea level altimetry products. *Ocean Science*, *15*, 1207–1224. https://doi.org/10.5194/os-15-1207-2019

Tapley, B. D., Bettadpur, S., Ries, J. C., Thompson, P. F., & Watkins, M. M. (2004). GRACE measurements of mass variability in the Earth system. *Science*, *305*(5683), 503–505. https://doi.org/10.1126/science.1099192

Tapley, B. D., Watkins, M. M., Flechtner, F., Reigber, C., Bettadpur, S., Rodell, M., et al. (2019). Contributions of GRACE to understanding climate change. *Nature Climate Change*, *9*, 358–369. https://doi.org/10.1038/s41558-019-0456-2

Tregoning, P., Lambeck, K., & Ramillien, G. (2008). GRACE estimates of sea surface height anomalies in the Gulf of Carpentaria, Australia. *Earth and Planetary Science Letters*, *271*(1–4), 241–244. https://doi.org/10.1016/j.epsl.2008.04.018

Weigelt, M. (2017). The acceleration approach. In M. Naeimi, & J. Flury (Eds.), *Global gravity field modeling from satellite-to-satellite tracking data, Lecture Notes in Earth System Sciences* (pp. 127–160). Cham, Switzerland: Springer International Publishing.

Wunsch, C. (2015). *Modern observational physical oceanography*. Princeton University Press.

Yu, Y., Chao, B. F., García-García, D., & Luo, Z. (2018). Variations of the Argentine Gyre observed in the GRACE time-variable gravity and ocean altimetry measurements. *Journal of Geophysical Research: Oceans*, *123*(8), 5375–5387.

Yuan, D.-N. (2019). *GRACE Follow-On JPL Level-2 processing standards document, for Level-2 product release 06, Jet Propulsion Laboratory*. California, USA: California Institute of Technology.

Zuber, M. T., Smith, D. E., Watkins, M. M., Asmar, S. W., Konopliv, A. S., Lemoine, F. G., et al. (2013). Gravity field of the Moon from the Gravity Recovery and Interior Laboratory (GRAIL) mission. *Science*, *339*(6120), 668–671. https://doi.org/10.1126/science.1231507

Reference From the Supporting Information

Google, Inc. (2022). Retrieved from http://maps.google.com/